Citation (APA)
Bol, R. J. M., Zhou, W., Meng, Z., Schlangen, E., & Šavija, B. (2026). Tailored Poisson's Ratio-reinforced Cementitious Composites for flexural applications. *Cement and Concrete Composites*, *168*, Article 106485. https://doi.org/10.1016/j.cemconcomp.2026.106485

Cement and Concrete Composites 168 (2026) 106485

Contents lists available at ScienceDirect

Cement and Concrete Composites

journal homepage: www.elsevier.com/locate/cemconcomp

Tailored Poisson's Ratio-reinforced Cementitious Composites for flexural applications

Rowin J.M. Bol [a],*, Wen Zhou [a,b],*, Zhaozheng Meng [a], Erik Schlangen [a], Branko Šavija [a]

[a] Microlab, Faculty of Civil Engineering and Geosciences, Delft University of Technology, Stevinweg 1, 2628 CN Delft, The Netherlands
[b] School of Civil and Environmental Engineering, Nanyang Technological University, 50 Nanyang Avenue, 639798, Singapore

ARTICLE INFO

Keywords:
Poisson's ratio
Auxetic
Cementitious composites
Polymeric reinforcement
3D printing
Flexural properties

ABSTRACT

The use of Additive Manufacturing (AM) to create reinforcements for cementitious composites has become a popular research topic in recent years. One illustrative example is the integration of 3D-printed auxetic reinforcements into cementitious matrices, which exhibit superior energy absorption due to their negative Poisson's ratio. This presents the opportunity to tailor the Poisson's ratio of reinforcements to align with local stress distributions and enhance structural efficiency. In this study, Tailored Poisson's Ratio-reinforcements (TPR) were proposed, characterized by a linear gradient of Poisson's ratios along the height of the reinforcement to accommodate varying stress profiles within beams. Specifically, the top chords of TPR exhibit negative Poisson's ratios (auxetic), undergoing lateral contraction under compression and providing confinement to the surrounded matrix. Conversely, the bottom chords possess positive Poisson's ratios, contributing to lateral contraction under tension. These lateral deformations cause a shift in the principal stress state of the confined matrix, extending the loading path in stress space and actively delaying failure. Three novel Tailored Poisson's Ratio-reinforced Cementitious Composite (TPRCC) designs are developed and tested under four-point bending in this study. Experimental recordings indicate increases in load capacity and toughness of up to 191% and 6900% with respect to plain mortar, respectively.

1. Introduction

The use of Additive Manufacturing (AM) to create reinforcements for cementitious composites has become a popular research topic in recent years [1–3]. Various AM techniques enable the construction of polymeric and metallic reinforcements, such as Fused Filament Fabrication (FFF) or Fused Deposition Modelling (FDM) [4–9], StereoLithogrAphy (SLA) [10–12], and Powder Bed Fusion (PBF) or Selective Laser Sintering (SLS) [13–15]. These processes can build structural designs having complicated geometries with virtually any shape, thereby potentially facilitating improved mechanical behaviour inconceivable in the past [16]. AM is thus a powerful tool which allows for tailored reinforcements providing optimal properties for cementitious composites. For instance, Dong et al. [17] describe various functionally graded lattice structures as reinforcement for cementitious composites which reached about 40 % to 50 % improvements in specific stiffness compared to uniform meshes. Clausen et al. [18] produced a novel class of architected materials having programmable Poisson's ratios between −0.8 and 0.8 which sustain under large deformations (i.e., up to 20 % strain). Stepinac & Galić [19] investigated optimized (functionally) graded auxetic cores for sandwich structures, only feasible through AM (i.e., FDM). Panesar et al. [20] derived functionally graded lattice structures for AM applications through topology optimization, whilst Xu & Šavija [21] created functionally graded lattice reinforcement for cementitious composites by means of 3D printing.

The symbiosis of 3D-printed polymeric architectures embedded in cementitious matrix has led to numerous favourable mechanical properties like enhanced strength, toughness, and energy absorption capacity [2,22]. One illustrative example of such composites are Auxetic Cementitious Composites (ACCs) [23]. ACCs use auxetic structures having a negative Poisson's ratio [24–38] as reinforcement in cementitious matrices. For virtually any common material [39], it usually gets thinner in cross-section when stretched through elongation [29, 31,32,40], e.g., an elastic band [29,40], as shown in Fig. 1(a). The same but opposite holds when compressing materials, as it 'extends itself in other directions' as observed for elastic gum by Thomas Young back in the 1800s [41]. The supposition that materials may have a negative Poisson's ratio dates back to more than a century ago, as it was discussed by Love [42]. This implies that longitudinal stretch produces lateral expansion and compression yields a reduction in cross-section [29,43,44], see Fig. 1(b). The term 'auxetic' was initially coined

---

* Corresponding authors.
E-mail addresses: R.J.M.Bol@tudelft.nl (R.J.M. Bol), wen.zhou@ntu.edu.sg (W. Zhou).

https://doi.org/10.1016/j.cemconcomp.2026.106485
Received 26 November 2025; Received in revised form 9 January 2026; Accepted 14 January 2026

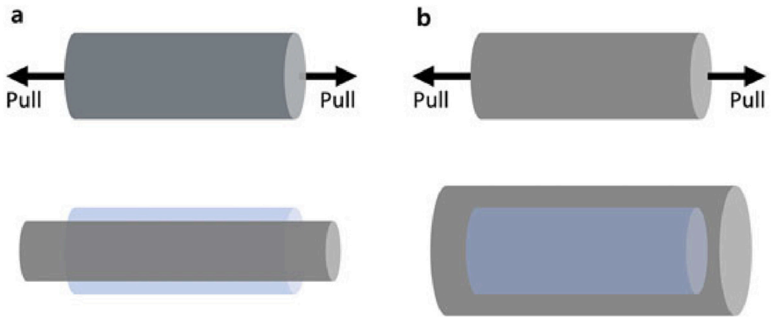

Fig. 1. Deformation of a rod under tension when its Poisson's ratio is (a) positive (as in ordinary materials) and (b) negative (as in auxetic materials) [31].

by Evans [40], who derived it from the Greek word 'auxetikos' which means 'that which tends to increase' [26,31]. Auxetics can be either natural or artificial [30], whereas the latter usually refers to auxetic metamaterials (man-made materials having properties that are unseen in natural materials [45]).

Various architectures are known for exhibiting auxeticity, such as re-entrant models [46–51], rotating unit mechanisms [28,31,32,35] and chiral mechanisms [38,45,52,53]. These auxetics are often praised in the literature for having extraordinary properties, e.g., high shear modulus, specific strength and fracture toughness; increased indentation resistance, damping and energy absorption; as well as synclastic bending curvature, changeable permeability, impact resistance, fatigue toughness and having a low weight [54–63]. When applied as reinforcement in cementitious composites, such as ACCs, excellent energy absorption capabilities can be achieved [23].

However, the development of ACCs mainly focuses on compressive applications [1,64]. Xu & Šavija [23] proposed novel ACCs that benefit from the outstanding compressive strength of cementitious materials while exploiting the large deformation capacity of polymeric Acrylonitrile Butadiene Styrene (ABS) auxetic architectures. Their findings show that all of the designed ACCs have excellent compressive ductility. Particularly the re-entrant and rotating-square structures exhibit lower Poisson's ratios compared to the others, such that these two ACC designs display better crack-arresting effect under compressive loads. As a result of these traits, the auxeticity of the re-entrant and rotating-square architectures provide more confinement to the cementitious matrix, such that similar compressive strength values as obtained for plain mortar are achieved by the ACCs. A very similar experimental and numerical study by Choudhry et al. [65], also using ABS auxetic designs in their Lattice-Reinforced Cementitious Composites (LRCCs), explored fracture patterns, compressive ductility and energy absorption capacity. Additionally, they investigate the effect of reinforcement ratio on the mechanical behaviour in compression in the range of 25 % to 40 %. Identical to Xu & Šavija [23], Choudhry et al. [65] conclude that the use of auxetic reinforcement in cementitious mortar changes the fracture behaviour from brittle to ductile. Again, the re-entrant design (LRCC 4 in [65]) showed the highest increase in ductility (i.e., over 200 %), which is attributed to the auxetic reinforcement's ability to hinder the matrix to shear, thereby actively restraining (micro-)crack propagation by means of bi-axial compression. The aforementioned publications both report small reductions in strength as a result of adding polymeric reinforcement, thereby illustrating a trade-off among strength and ductility. Although other studies have found ductility to increase together with strength [3,66,67], it remains unknown how to balance these mechanical properties.

Most studies on ACCs have only limited attention for tension and bending [68–71], albeit promising. Cementitious materials are known to have a low tensile strength, fracture toughness and ductility [70]. Hence, the latter reference lists some of the efforts to overcome these issues, such as fiber-reinforcement that can improve structural ductility. In their work, architected composites have been developed by combining cement mortar with an ABS polymer phase, thereby imitating the microstructure of nacre. They found that these composites outperformed control specimens. If flexural auxetic reinforcement is implemented, it is mostly oriented in-plane (i.e., the auxetic deformation mechanisms occur in the same plane as the loading) [1,70,72]. Particularly, cementitious composites with re-entrant auxetic reinforcements accomplish promising strength and ductility values when subjected to compression and bending [71]. Few publications tested ACCs where the auxetic response of the reinforcement takes place out-of-plane (e.g., [68]). Current flexural studies on cementitious composites consider planar [2,6,68–70,73,74] as well as three-dimensional [17,75,76] reinforcement designs. Planar reinforcement is often implemented in thin beams resulting in high reinforcement ratios [6,68]. Other configurations, including three-dimensional reinforcements, seek to achieve a flexural hardening response with volume fractions ranging from 20 % up to 50 % [2,17,77,78]. Nevertheless, examples with lower reinforcement ratios exist that exhibit flexural softening [69]. More recently, Zhou et al. [79] investigated the flexural behaviour of LRCCs with considerably small volume fractions (2.5 % to 3.8 %). Therein, all LRCCs reached flexural strengths that were roughly the same as the reference mortar, even though significant increases in energy absorption capacities were reported (500 % to 2300 %). On the other hand, flexural applications of Architected Polymer-Concrete Composites (APCCs) containing significantly higher reinforcement ratios (∼80.7 %) have also been reported that exhibit strain hardening behaviour [74]. The latter reference argues in favour of polymeric reinforcements in view of their low mass and high corrosion resistance, as well as the APCCs' potential for upscaling to practical applications. It was observed that the mechanical behaviour of the APCCs is dependent on the reinforcement's geometry and dimensions, which were optimized to maximize specific flexural strength and toughness. The optimization process involved sequential surrogate modelling using Finite Element Analysis (FEA) in which the constitutive relationships for the cementitious matrix and ABS reinforcement were implemented through a Concrete Damaged Plasticity Model (CDPM) and multi-linear ductile material model. The bond amongst the two materials was modelled via 'embedded region', assuming a fully perfect bond. However, experimentally observed damage mechanisms revealed that debonding, shown by horizontal cracking, assisted in diminishing strain levels through (re)distribution over increased lengths. As a result, stress concentrations were reduced, thereby restraining crack propagation and increasing the energy dissipation capacity.

Research on the bond between ABS polymer and cementitious material is scarce, leading [70] to study the effects of interfacial properties and bond strength between ABS and cement paste. The authors' preceding research [80] also focused on the effects of auxetics. As pointed out in both studies, interlocking and friction between the plastic and cementitious matrix contributes to the distribution of deformation, thereby enabling the occurrence of plastic deformation after initial cracking [70]. This interlocking enhanced strength and stiffness [80]. Xu et al. [81] performed pull-out tests to quantify the bond strength of the ABS-mortar interface. They recorded bond strengths of only a few MPa, which were attributed to the hydrophobic nature of ABS. Hence, there is a lack of chemical bond (i.e., adhesion) with the matrix, such that the bond relies mainly on frictional contributions. Moreover, Bol et al. [82] studied the influence of surface roughness as a result of the FDM 3D printing technique on the ABS-matrix bond. They found that the bond strength can increase up to 56 % depending on the printing configuration, further emphasizing its importance.

Auxetic behaviour may enhance the frictional bond among the two materials as described in several works (e.g., [31,35,40]) for fiber-reinforced composites: If auxetic fibers are embedded in a cementitious matrix, these will expand under tension when the matrix fails. As a result, the pull-out resistance increases [31], thereby improving its energy absorption capacity [40]. Similar effects are applied in fasteners [31,40,55] and medical bone-screws [38,53]. In ordinary Reinforced Concrete (RC) beams subjected to downward bending, the bottom reinforcement adopts the stresses in the tensile region whilst the reinforcement at the top mitigates cracking and enhances stiffness in the compression zone [16]. However, it is questionable whether lateral expansion of auxetic bending reinforcement deteriorates the load-bearing capacity, particularly in the lower region subjected to tension. On the other hand, the reinforcement's deformation mechanism will bring the mortar in a state of biaxial compression in the upper zone, which is beneficial in terms of both strength and ductility [16,35]. More recent works concerning ACCs focus on the latter application, in which lateral confinement is an important factor [1].

This contradiction raised the idea to tailor the Poisson's ratio of the reinforcement according to the bending stress–strain distribution, meaning that the reinforcements in this study have a through-thickness gradient of Poisson's ratio that is aligned with the elastic bending stress distribution, distinguishing it from previous architected reinforcements with uniform Poisson's ratio. It is thereby the aim to laterally confine the cementitious matrix throughout its maximally stressed locations. The hypothesis is that Tailored Poisson's Ratio-reinforcement (TPR) will cause a shift in the principal stress state, leading to an extended loading path in stress space, actively postponing failure of the surrounded matrix. The top chord of the reinforcement will be auxetic, resulting in lateral confinement under compressive strain. In contrast, the bottom chord receives a positive Poisson's ratio, providing lateral compressive stress when loaded in tension. The neutral axis has a Poisson's ratio that is virtually zero, such that it varies linearly over the height. A similar conceptualization is envisioned by Vitalis et al. [16] for Interpenetrating Phase Composite (IPC) beams in a RC frame. However, their conceptualized (auxetic) lattice bending reinforcement is yet again oriented in-plane, such that it cannot accommodate continuous confinement pressure over the height of the beams. In contrast, our proposed out-of-plane TPR is continuous, allowing for lateral confinement throughout the height of the beam.

The literature shows that prior work has mainly focused on compression or in-plane applications of auxetic reinforcement, often at high reinforcement ratios. Moreover, experimental explorations of reinforcement with a tailored Poisson's ratio to align with local stress distributions in flexure are currently lacking, especially out-of-plane lattices at low reinforcement ratios. The main objectives of this work are therefore as follows:

1. To design 3D-printed reinforcements with a prescribed gradient in Poisson's ratio suitable for flexural applications.
2. To experimentally assess the flexural behaviour of these reinforcements and corresponding reinforced cementitious composites.
3. To evaluate the hypothesized lateral confinement mechanism and its impact on load capacity and toughness.

To this end, three Tailored Poisson's Ratio-reinforced Cementitious Composite (TPRCC) designs having a relatively low reinforcement ratio (14.6 % to 14.7 %) are developed and tested. Experimental recordings indicate increases in load capacity and toughness of up to 191 % and 6900 % with respect to plain mortar, respectively. CT scans after testing reveal the fracture behaviour and key interfacial phenomena (e.g., debonding and load transfer) of the considered TPRCCs.

2. Experimental details

2.1. Tailored Poisson's Ratio-reinforcement (TPR)

The Tailored Poisson's Ratio-reinforcement (TPR) designs developed in this work are based on common auxetic and non-auxetic unit cell geometries from literature having varying deformation mechanisms. The novelties of our proposed TPR designs are: (i) orienting the flexural auxetic reinforcement out-of-plane (i.e., the auxetic deformation mechanisms occur in the plane perpendicular to the loading) instead of in-plane, and (ii) rather than having planar reinforcement geometries and constant Poisson's ratios along the height, here the geometries gradually change to have a linear gradient of Poisson's ratios for accommodating varying stress profiles within beams. Therefore, each unit cell geometry is selected from literature based on the following requirements:

1. Unit cell geometries should exhibit a similar Poisson's ratio in tension and compression.
2. The geometry of the unit cell should be highly porous so that cementitious matrix can easily fill the gaps.
3. A pair of corresponding auxetic and non-auxetic unit cell geometries should share the same deformation mechanism.
4. Similar unit cell geometries should be available in a wide range of Poisson's ratios or adjustable to possess a prescribed Poisson's ratio.

The first geometry meeting all of the aforementioned criteria is based on Gibson's model [35,46,47] and named after honeycomb arrangements of Re-Entrant (RE) models, see Fig. 2. In this study, square unit cells are considered having dimensions of $h = l = 18\,\mathrm{mm}$, providing enough space for cementitious mortar to flow in. Similarly to Li et al. [35], the RE unit cell geometries can be adjusted to possess an assumed and prescribed theoretical Poisson's ratio, ν, by computing $\theta = \arctan \nu l/h$, $H = (h - l \tan\theta)/2$ and $L = l/2\cos\theta$. In Fig. 2, the top RE figure illustrates a traditional honeycomb with a positive Poisson's ratio and the bottom RE figure displays a re-entrant shape that is auxetic. The second geometry concerns a combination of two rotational designs discussed in [38,83], referred to as star structure (positive Poisson's ratio) and 3D cross-chiral structure (auxetic), also referred to as Rotating Square (RS) [9,22,23,79] in Fig. 2. In this case, the unit cell geometry varies similar to RE (i.e., by altering the internal strut angles), provided that two of the four internal strut angles that are opposite must remain re-entrant. The final geometry in Fig. 2 considers nine Topology Optimized (TO) architectures with programmable Poisson's ratios that are strain-independent (i.e., nearly constant over large deformations) in the range of $-0.8 \leq \nu \leq 0.8$ by Clausen et al. [18]. This was achieved through the application of a geometrically non-linear model, elaborated by Sigmund and coworkers [84], in an optimization framework aiming to minimize the discrepancy among real and prescribed Poisson's ratios for nominal strains at intervals until 20 %.

The selected unit cell geometries in Fig. 2 formed the basis for the three TPR designs shown in Fig. 3. The TPR unit cell geometry based on RE varies linearly over the height in agreement with the theoretical Poisson's ratio $-0.5 \leq \nu(Z) \leq 0.5$, such that the top is auxetic ($\nu(36) = -0.5$) and the bottom has a positive Poisson's ratio ($\nu(0) = 0.5$). The neutral axis has a Poisson's ratio that is virtually zero (i.e., $\nu(18) = 0$). Similarly, the TPR RS unit cell design is constructed by linearly interpolating its horizontal cross-sections over the height in accordance with $-0.5 \leq \nu(Z) \leq 0.5$. To end up with a continuous reinforcement layout, the nine unit cell curves corresponding to TO were vertically

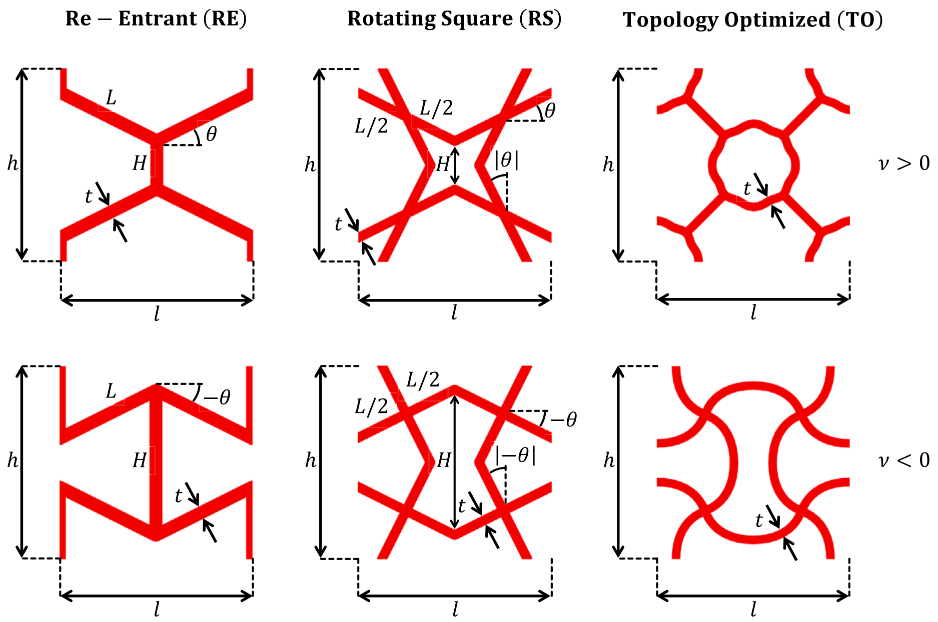

Fig. 2. Unit cell geometries. Parameters h and l are the unit cell dimensions; H is the length of vertical cell walls or vertical distance between inclined cell walls and L the length of the inclined cell walls; t the thickness of the cell walls; θ the inclination angle, which is negative for $\nu < 0$.

Table 1
Printing process parameters for Tailored Poisson's Ratio-reinforcement (TPR).

Printing parameters	Configurations
Layer height (mm)	0.2
Nozzle size (mm)	0.4
Wall thickness (mm)	0.4
Wall line count	2
Horizontal expansion (mm)	0.01
Infill density (%)	100
Printing temperature (°C)	245
Build plate temperature (°C)	85
Flow (%)	120
Print speed ($\mathrm{mm\,s^{-1}}$)	60

distributed over the height of 36 mm through which a lofted surface was created by means of Rhinoceros® using Grasshopper. The strut widths are different to ensure a comparable reinforcement ratio among the designs. Please note that the Poisson's ratio distributions in Fig. 3 are theoretical, based on analytical and topology optimized unit cell models, and not measured in this work. The TPR designs were manufactured by an Ultimaker S5 commercial FDM 3D printer using Ultimaker ABS material (ø2.85 mm, 750 g) as polymer filament. The printing process parameters are provided in Table 1 and the build orientation was along the height (Z in Fig. 3). Due to the maximum strut width of 1.2 mm for RE, the nozzle size being 0.4 mm and a wall line count (number of perimeters) of 2 did not require infill patterns during FDM printing.

2.2. Four-point bending tests of Tailored Poisson's Ratio-reinforcement (TPR)

To have more insight into the TPR's flexural behaviour, the ABS 3D prints were first subjected to four-point bending tests without cementitious matrix. All designs are composed of 8 × 2 unit cells and each TPR was tested in two configurations: UpRight (UR) and Upside Down (UD), see Fig. 4. The six resulting TPR layouts allow for comparison in mechanical properties considering the variation in both the theoretical Poisson's ratio and horizontal cross-sectional area over the height (see Fig. 3) for the 3D prints and eventually for the composites. UR samples are auxetic at the top and have a positive Poisson's ratio at the bottom, whilst UD samples have a positive Poisson's ratio at the top and are auxetic at the bottom. Each TPR design was tested twice in the UR and UD configurations, which adds up to a total of 12 samples. Fig. 4 further shows that small legs were added to correctly position the TPR ABS 3D prints in the mould to later casting the composites.

Fig. 5 shows the experimental setup. The TPR ABS samples were loaded to bend at a constant displacement rate of $0.02\,\mathrm{mm\,s^{-1}}$ by a hydraulic press INSTRON 8872. The loading pins have a diameter of 10 mm and were not lubricated. During the test, the load was recorded directly by the device itself whilst a Linear Variable Displacement Transducer (LVDT) was used to measure the cross-head displacement which did not observe machine compliance, see Fig. 5.

2.3. Four-point bending tests of Tailored Poisson's Ratio-reinforced Cementitious Composite (TPRCC)

Similar to the four-point bending tests of the TPR ABS 3D prints, the experiments regarding the Tailored Poisson's Ratio-reinforced Cementitious Composite (TPRCC) designs comprise six layouts denoted by UR and UD as shown in Fig. 6. Each TPRCC design was tested three times in both the UR and UD configuration, resulting in a total of 18 samples. Prior to casting the cementitious matrix, the small additional legs of the TPR ABS 3D prints were glued to the bottom of styrofoam moulds to prevent floating. Given the location of these legs, all TPR prints were cast in their upside-down configuration (see Fig. 7). Nonetheless, each TPRCC design was tested in UR and UD configuration, see Fig. 6. No surface preparation nor post-treatment of the ABS was used before casting. Similar to the TPR, the six resulting TPRCC layouts allow for comparison in mechanical properties considering the variation in both the theoretical Poisson's ratio and horizontal cross-sectional area over the height (see Fig. 3). The final TPRCC samples have dimensions of 160 × 40 × 40 mm such that the TPR has a cover of at least 2 mm, see Fig. 8. This resulted in reinforcement ratios of 14.6 % to 14.7 %.

The cementitious matrix consists of ordinary Portland cement (CEM I 42.5N) and fly ash as binders, silica sand (0.125–0.250 mm) as fine aggregate, and superplasticizer (Glenium 51) to tailor its rheology. The mix design, having water-to-binder and sand-to-binder ratios of 0.40 and 0.46, respectively, is provided in Table 2. The mixing process initiated by pre-mixing the dry ingredients for 2 min, followed by adding and mixing the water and superplasticizer for an additional 4 min.

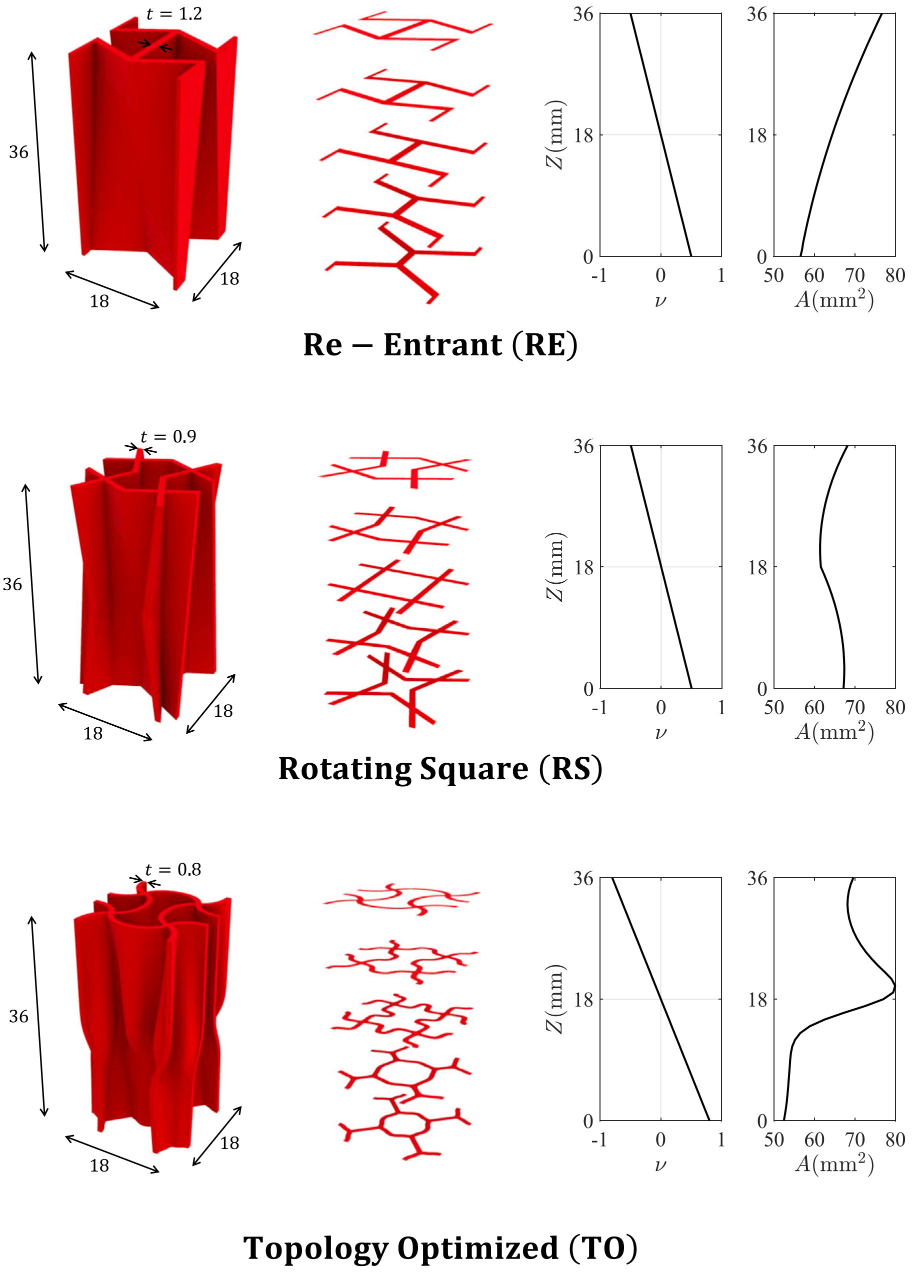

Fig. 3. Tailored Poisson's Ratio-reinforcement (TPR) designs. From left to right: Unit cell dimensions (mm), horizontal cross-sections, theoretical Poisson's ratio (ν) over height (Z), and horizontal cross-sectional area (A) over height (Z). Strut widths are constant over the height.

Once the cementitious matrix was cast into the moulds, these were put on a vibration table for 30 s. Demolding of the TPRCC specimens took place after 48 h and these were moved to a curing room for 26 d (temperature 20 ± 2 °C, humidity 96 ± 2 %) to be tested after 28 d in total. The same matrix has been experimentally characterized at similar age in previous works by the authors [23,79] and corresponds to a compressive strength of 24 MPa, flexural strength of 3.5 MPa and modulus of 10 105 MPa.

Analogous to the TPR ABS 3D prints, four-point bending tests of the six TPRCC layouts are used to compare the flexural behaviour and test the TPR's hypothesized lateral confinement mechanism given their varying Poisson's ratio and cross-section over the height (Fig. 3). The UR configurations will show the effects of reinforcements having strain-tailored Poisson's ratios according to the bending stresses. UD configurations are expected to perform worse since these would cause lateral expansion, thereby deteriorating the composite's mechanical properties. Fig. 9 depicts the same experimental setup, now loading a TPRCC specimen in bending at $0.02\,\mathrm{mm\,s^{-1}}$ using a LVDT to record the machine displacement.

Table 2
Mixture design.

Mixture components	Quantities (g L^{-1})
CEM I 42.5N	473
Fly ash	559
Sand (0.125–0.250 mm)	473
Water	413
Superplasticizer (Glenium 51)	2.0

Before testing, a side surface for each of the TPRCC specimens was covered with white paint and sprinkled with black dots for 2D Digital Image Correlation (DIC) analysis to study their exterior cracking

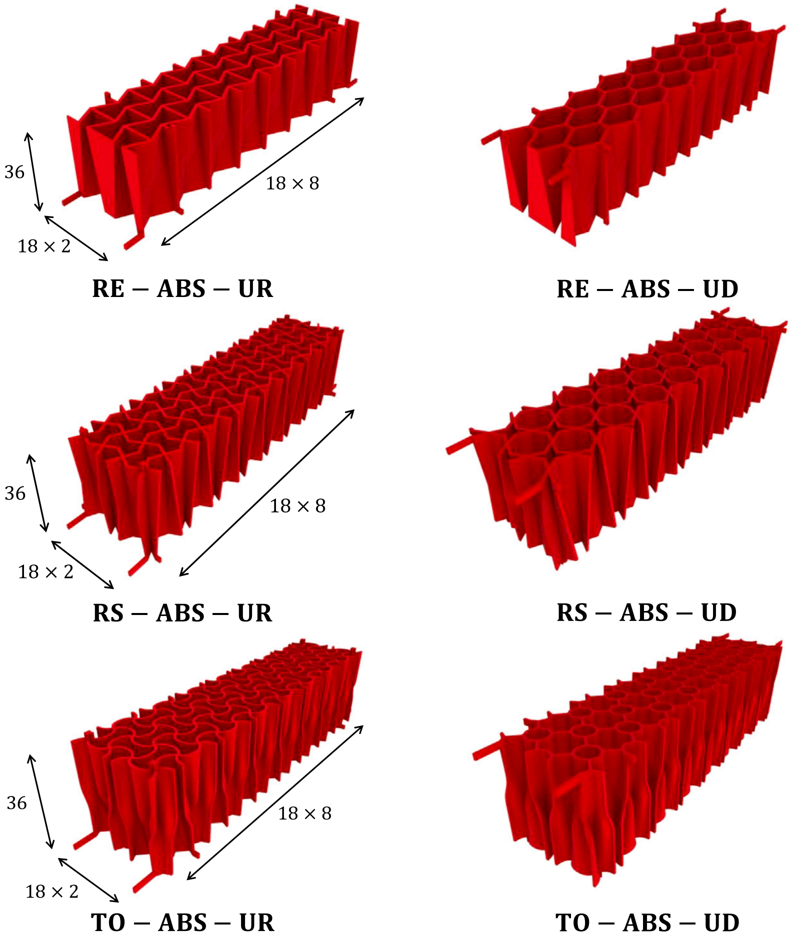

Fig. 4. Tailored Poisson's Ratio-reinforcement (TPR) ABS 3D prints (unit: mm). Each design has two configurations: UpRight (UR) and Upside Down (UD).

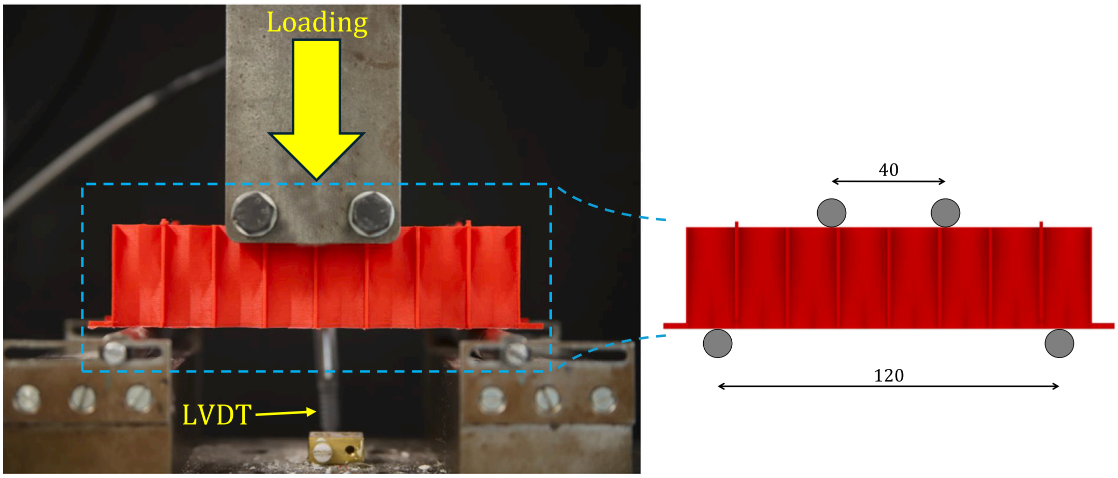

Fig. 5. Experimental setup for TPR ABS specimens (unit: mm).

patterns. A Canon EOS 6D Mark II digital camera was positioned 600 mm away from the specimen surface to acquire high-resolution images throughout the tests. The camera was equipped with a 75 mm focal length lens and operated at an aperture of $f/2.8$. Images were captured at a resolution of 6240 × 4160 pixels and analysed in the software ZEISS INSPECT Correlate. Moreover, since the hypothesized lateral contraction mechanism occurs inside the unit cells of the TPR, X-ray micro Computed Tomography (XCT) scans were made to visualize the internal state of damage in the TPRCC samples. During testing, all specimens were loaded until ultimate failure. One of each UR and UD configurations of the TPRCC designs were selected to be scanned by a TESCAN CoreTOM μ-CT scanner, operated at a tube voltage of 120 kV and a current of 125 mA. In view of the specimen's dimensions, a Region Of Interest (ROI) was considered at mid-span where the bending moment is maximum and constant (i.e., in between the two point loads). The sequentially acquired 4283 projections (number of slices) of the damaged samples were reconstructed using StudioMax software and visualized in Dragonfly software at a resolution of 15 μm.

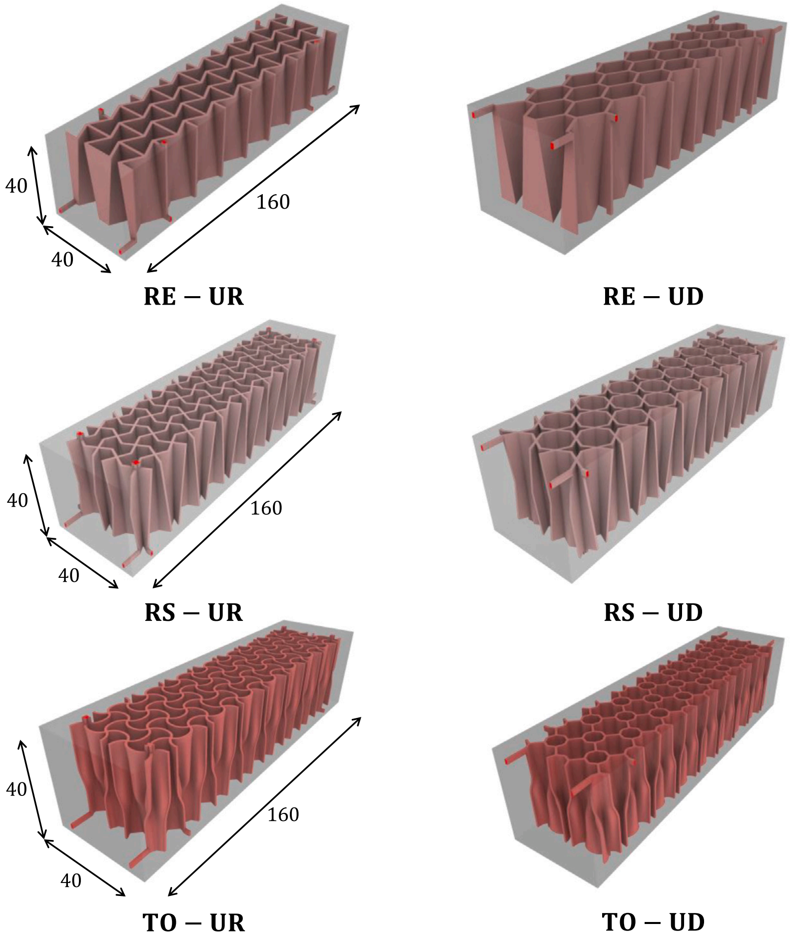

Fig. 6. Tailored Poisson's Ratio-reinforcemed Cementitious Composite (TPRCC) specimens (unit: mm). Each design has two configurations: UpRight (UR) and Upside Down (UD).

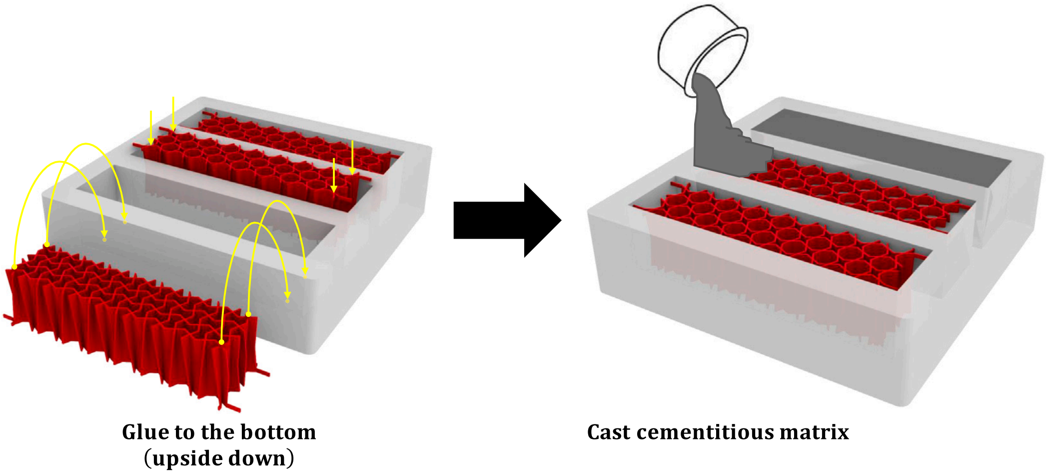

Fig. 7. Specimen preparation and casting procedure.

3. Results and discussion

3.1. Flexural behaviour of Tailored Poisson's Ratio-reinforcement (TPR)

The load–displacement curves, deformation and fracture patterns of the six TPR layouts are displayed in Fig. 10. All experiments show a high level of consistency among the tested samples, particularly in the linear-elastic regime. Only at larger displacements, more deviations in mechanical response occur.

Fig. 10(a–c) show that the TPR ABS 3D prints exhibit comparable load capacities among UR and UD configurations, despite their differences in horizontal cross-sectional area over the height (see Fig. 3). RE-ABS designs (Fig. 10(a)) display the greatest peak load and stiffness, followed by RS-ABS (Fig. 10(b)) and TO-ABS (Fig. 10(c)) in decreasing order, see Fig. 11(a). Error bars represent the standard deviation. Note

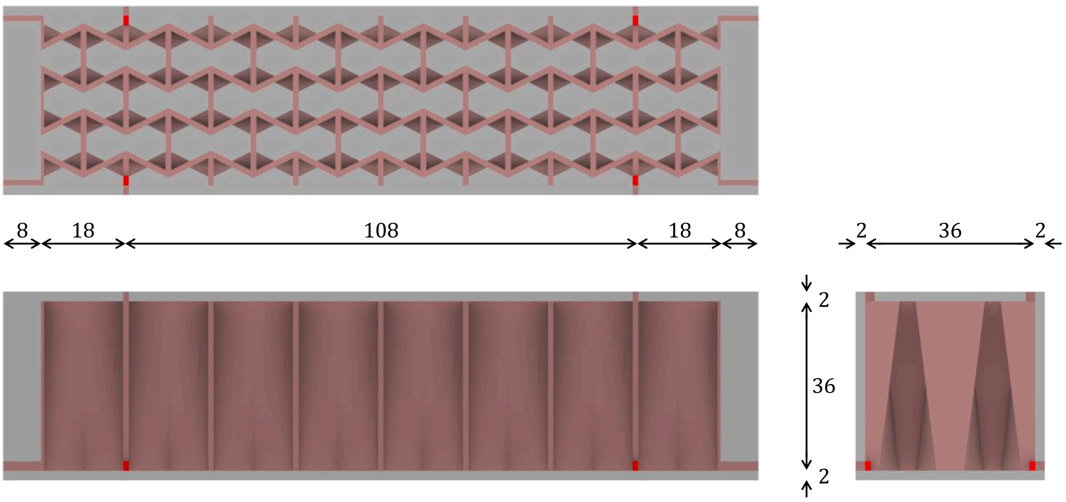

Fig. 8. TPRCC specimen dimensions (unit: mm).

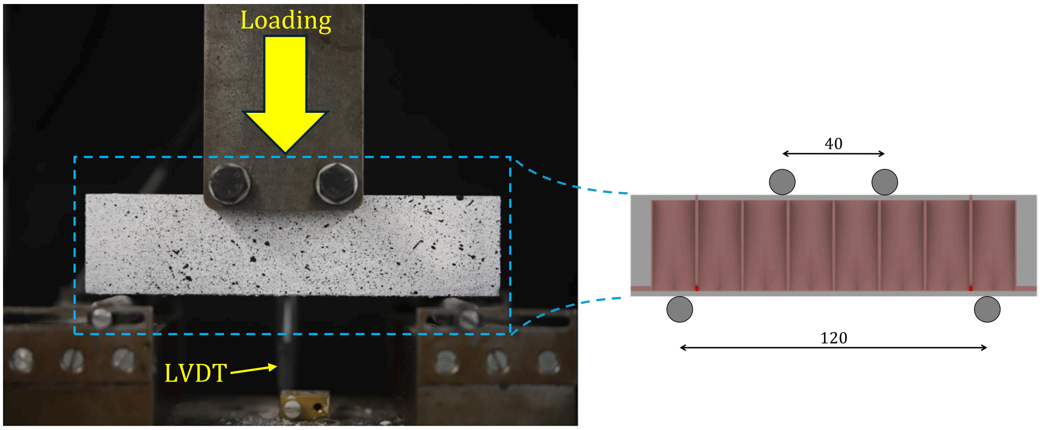

Fig. 9. Experimental setup for TPRCC specimens (unit: mm).

Table 3
Flexural properties of TPR ABS 3D prints.

TPR ABS 3D print	Load capacity (kN)	Toughness (J)
RE-ABS-UR	1.4467 ± 0.0850	8.4696 ± 0.9867
RE-ABS-UD	1.4957 ± 0.0277	5.0143 ± 0.4438
RS-ABS-UR	1.1768 ± 0.0332	5.1208 ± 0.2665
RS-ABS-UD	1.0783 ± 0.0238	4.2894 ± 0.2071
TO-ABS-UR	0.8627 ± 0.1015	14.8988 ± 3.2812
TO-ABS-UD	0.9074 ± 0.0735	13.4017 ± 4.3857

that for TO-ABS-UR the first local maximum is considered as load capacity. When looking at Fig. 3, it can be observed that the TPR load capacity and stiffness are positively associated with their strut thickness. In terms of toughness, measured as the area underneath the load–displacement curve [74] until ultimate failure of the samples, TO-ABS significantly outperforms the others, with RS-ABS performing the worst (Fig. 11(b)). A summary of flexural properties of TPR ABS 3D prints, including standard deviations, is provided in Table 3. Both Fig. 11(a) and Table 3 exemplify a small variability in the observed load capacities of each TPR design with differences between the UR and UD configurations below the experimental scatter.

Remarkably, the TPR ABS 3D prints seem to only possess post-peak load-bearing capacity if the horizontal cross-sectional area increases with respect to its value at the bottom. Fig. 12 plots the horizontal cross-sectional area over the height for all TPR design configurations, wherein it can be seen that only for RE-ABS-UR, TO-ABS-UR and TO-ABS-UD this is the case. This is evidenced by Fig. 10(a) and (c).

Furthermore, Fig. 10(d–i) display typical fracture patterns for all TPR ABS 3D prints: Cracking initiates vertically, up to the position where the unit cell geometry becomes rectangular, followed by horizontal delamination, caused by inter-layer failure as a result of the printing path-dependent anisotropy present in FDM 3D printed polymers [9]. For RE-ABS and RS-ABS, the rectangular cross-section is located at the neutral axis (i.e., halfway up the beam where $v = 0$, see Fig. 3). However, in TO-ABS this transition takes place at $v = 0.2$ as defined for the nine reference architectures by Clausen et al. [18]. This difference originates from the geometrically non-linear model by Sigmund and co-workers [84] used to derive the strain-independent architectures, whereas RE and RS are based on linear designs. Hence, the horizontal crack is slightly shifted downwards for TO-ABS-UR (Fig. 10(h)) whilst it occurs somewhat higher in TO-ABS-UD (Fig. 10(i)).

The TPR load capacities can be related to the printing path-dependent anisotropy inherent to FDM 3D printed polymers [9]. Fig. 13 shows bottom views of the tested TPR specimens. RE-ABS exhibited the highest load capacity (Figs. 10(a) and 11(a)) and suffered from pure strut failure due to stress concentrations at its sharp corners (see Fig. 13(a) and (d)). Therefore, failure occurred in the direction of the filament (i.e., the bead direction) which is the strongest [9]. RS-ABS yielded a lower load capacity (Figs. 10(b) and 11(a)) and displayed a mixed failure mode. Similar to RE-ABS, RS-ABS mostly failed at its struts (again near the joints), but also showed some vertical

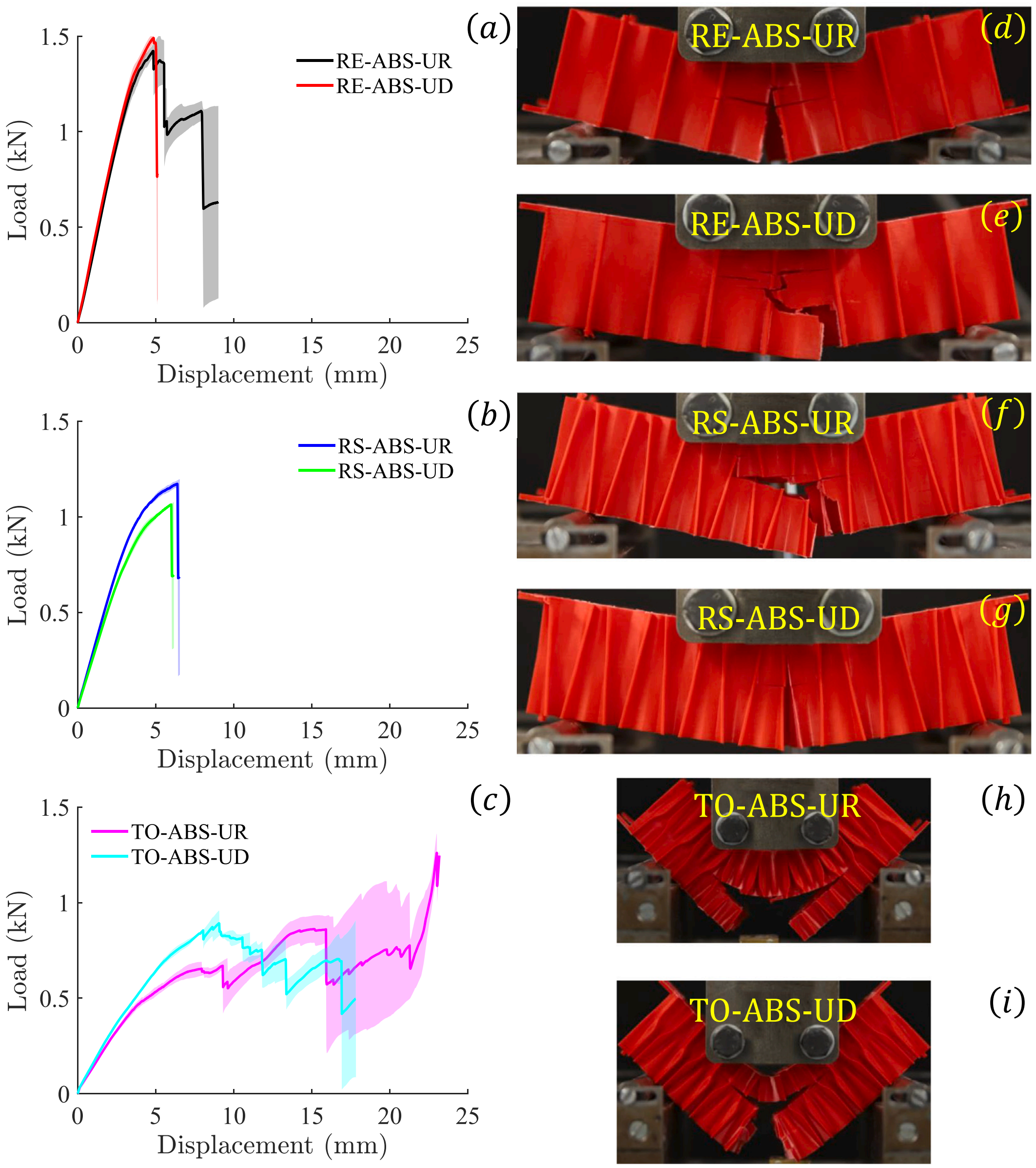

Fig. 10. Flexural behaviour of TPR ABS 3D prints: (a–c) Load–displacement curves, (d–i) deformation and fracture patterns. Note: (d,f,h) UR, (e,g,i) UD. The shaded areas represent the variations across parallel testing, and the solid lines represent the average results.

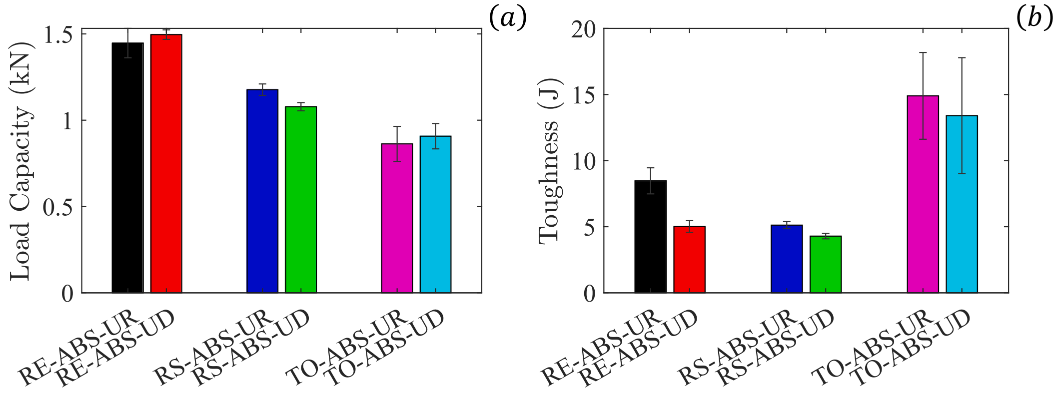

Fig. 11. Flexural properties of TPR ABS 3D prints: (a) Load capacity, (b) toughness.

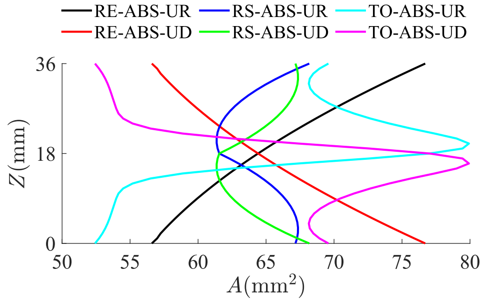

Fig. 12. All TPR unit cell horizontal cross-sectional areas (A) over height (Z).

delamination among neighbouring filaments (i.e., intra-layer failure), see Fig. 13(b) and (e). Bol et al. [9] found that the latter is weaker compared to the bead direction, which explains the lower load capacity of RS-ABS. TO-ABS reached the lowest peak load (Figs. 10(c) and 11(a)) and illustrated the same failure behaviour as RS-ABS. However, TO-ABS samples contained significantly more intra-layer delamination and less strut failure, probably because of their lack of sharp angles (see Fig. 13(c) and (f)). This explains TO-ABS' lowest load capacity.

Finally, Fig. 14 illustrates how the auxetic top chords of the RE-ABS-UR and TO-ABS-UR specimens undergo lateral contraction during loading. Through comparison of Fig. 14(a) and (c) as well as Fig. 14(b) and (d) for RE-ABS-UR and TO-ABS-UR, respectively, it can be clearly observed that the TPR designs exhibit more lateral contraction as a result of increasing compressive bending strains for larger vertical displacements.

Based on the four-point bending tests of the TPR layouts, the following flexural characteristics could be observed:

1. *Reinforcement load capacities are comparable among UR and UD configurations.* Despite their differences in horizontal cross-sectional area over the height, see Fig. 3.
2. *Reinforcement load capacity and stiffness are positively associated with strut thickness.* RE has the largest strut thickness (t = 1.2 mm), load capacity and stiffness. RS (t = 0.9 mm) shows intermediate values for all of these properties. TO, having the smallest strut thickness (t = 0.8 mm), scores lowest when it comes to peak load and stiffness. From all the measured flexural properties, only toughness does not follow the aforementioned trend. This mechanical performance is mainly affected by the failure mode of the TPR designs.
3. *Reinforcement only has post-peak load-bearing capacity if the horizontal cross-sectional area increases with respect to its value at the bottom.* This is only the case for RE-ABS-UR, TO-ABS-UR and TO-ABS-UD as shown in Figs. 10(a–c) and 12.
4. *Reinforcement load capacity can be related to failure mode.* RE-ABS specimens suffered from pure strut failure in the direction of the filament (i.e., the bead direction) which is the strongest print configuration, resulting in the highest load capacity. RS-ABS displayed a mixed failure mode of strut failure near joints and vertical delamination among neighbouring filaments (i.e., intra-layer failure). This yielded intermediate load capacity, because the intra-layer print configuration is weaker. TO-ABS mainly contained intra-layer delamination with minor strut failure, explaining its lowest load capacity.
5. *3D printed reinforcements show printing path-enabled horizontal crack deflection.* The typical fracture pattern initiates vertically, up to the position where the unit cell geometry becomes rectangular, followed by horizontal delamination, caused by inter-layer failure as a result of the printing path-dependent anisotropy present in 3D printed polymers.

Table 4
Flexural properties of TPRCC specimens.

TPRCC specimens	Load capacity (kN)	Toughness (J)
RE-UR	5.6147 ± 0.5212	10.9133 ± 2.4381
RE-UD	3.9610 ± 0.3791	10.3342 ± 2.1699
RS-UR	3.7213 ± 0.1671	9.9797 ± 0.7280
RS-UD	1.9942 ± 0.1365	5.7959 ± 0.7427
TO-UR	3.5151 ± 0.2524	15.6095 ± 1.0669
TO-UD	2.7116 ± 0.1092	24.0450 ± 0.7623
REF	2.1976 ± 0.0964	0.3584 ± 0.0074

3.2. Flexural behaviour of Tailored Poisson's Ratio-reinforced cementitious composite (TPRCC)

3.2.1. Mechanical performance

The load–displacement curves, deformation and fracture patterns of the six TPRCC layouts are shown in Fig. 15. Similar to the flexural TPR tests, all TPRCC specimens behave strikingly consistent, also at substantially larger displacements.

Fig. 15(a–c) illustrate that the TPRCC-UR specimens have significantly higher load capacities with respect to their UD counterparts. RE-UR (Fig. 15(a)) exhibits load capacities of more than 6 kN, which is an improvement of 191 % with respect to the plain reference mortar (REF, see Fig. 16(a)). RE-UD has a significantly lower load capacity, reaching only about 4 kN (Figs. 15(a) and 16(a)), although their toughness values are very close (Fig. 16(b)). RS-UR (Fig. 15(b)) performs slightly less than RE-UD in both load capacity and toughness, as shown in Figs. 16(a) and (b). Similarly, RS-UD (Fig. 15(b)) yields a lower load capacity compared to RS-UR (see Fig. 16(a)). TO-UR (Fig. 15(c)) has a somewhat lower load capacity with respect to RS-UR (see Fig. 16(a)), but gained more than 1.6 times the toughness (see Fig. 16(b)). This is an increase of more than 4700 % with respect to the plain reference mortar (see Fig. 16(b)). Following the same trend, Figs. 15(c) and 16(a) show that the load capacity of TO-UD is lower than TO-UR. However, TO-UD displays toughness values of nearly 25 J, thereby drastically increasing the energy absorption capacity by 6900 % compared to the plain reference mortar (see Fig. 16(b)). A summary of flexural properties of TPRCC specimens, including standard deviations, is provided in Table 4. Both Fig. 16(a) and Table 4 exemplify a small variability in the observed load capacities of each TPRCC design with differences between the UR and UD configurations significantly above the experimental scatter.

Fig. 15(d–i) also illustrate the TPRCC fracture patterns. Most specimens show a single major crack somewhere in the constant bending moment region, except for the TO-UD layout having consistently two main cracks below the points of load application (see Fig. 15(i)). Nonetheless, all tested samples exhibit multiple cracking behaviour, indicating their ability to redistribute bending stresses. This can be seen by looking at the small load drops in the first mm of displacement plotted in Fig. 17. RS has limited multiple cracking, followed by RE and TO in increasing order, directly correlated to their toughness values in Fig. 16(b).

Analogous to TPR, the TPRCC load capacities can be related to the printing path-dependent anisotropy of the 3D printed reinforcement in a similar manner. Fig. 18 shows bottom views of the tested TPRCC specimens, wherein RE (Fig. 18(a) and (d)) again suffered from pure strut failure in the strongest printing direction [9] reflecting the highest load capacity in Fig. 15(a). However, RS and TO (Fig. 18(b–c) and (e–f)) only showed vertical delamination between adjacent filaments (i.e., intra-layer failure), which is weaker [9] and thus produces relatively close load capacities (see Fig. 16(a)). However, especially TO-UD (Fig. 18(f)) displayed significantly more intra-layer delamination, relating to the astonishing high toughness in Fig. 16(b). Hence, the printing path-dependent anisotropy of TPR seems to be the limiting factor in the developed TPRCC specimens.

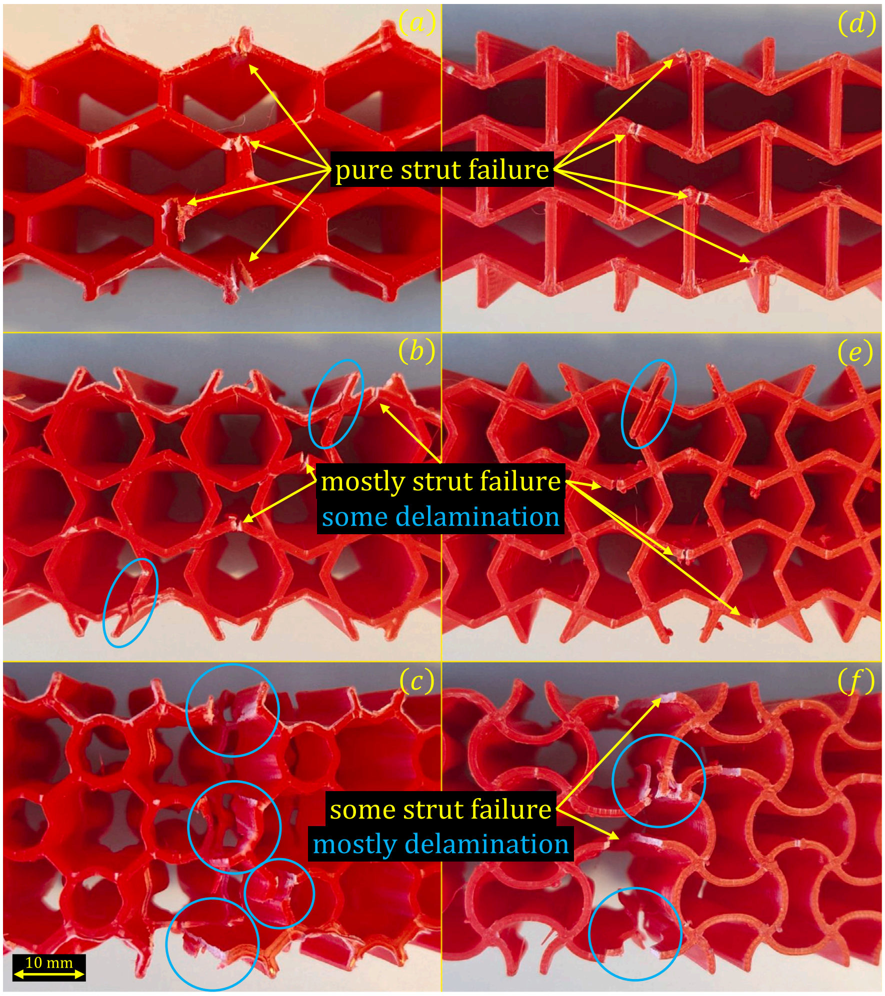

Fig. 13. Failure modes of TPR ABS 3D prints: (a) RE-ABS-UR, (b) RS-ABS-UR, (c) TO-ABS-UR, (d) RE-ABS-UD, (e) RS-ABS-UD, (f) TO-ABS-UD. Note: (a–c) bottom views of UR configurations, (d–f) bottom views of UD configurations.

Since the TPR ABS 3D prints exhibit comparable load capacities among UR and UD configurations (Figs. 10(a–c) and 11(a)), the difference in TPRCC-UR and TPRCC-UD load capacities are consistent with the hypothesized lateral confinement mechanism present in UR, which is absent in UD. Fig. 19(a) displays the principal stress state for plain reference mortar, without lateral confinement. In this scenario, the top chord would fail in uniaxial compression, see the left side of Fig. 19(a), whilst the bottom chord would fail in uniaxial tension as plotted on the right side of Fig. 19(a). However, as shown in Fig. 19(b) for RE-UR, the auxetic re-entrant reinforcement in the top chord provides lateral confinement under compressive strain. Therefore, the failure state in the upper region of the cementitious matrix gets shifted from a more or less uniaxial compression towards a minor biaxial compression stress state, see the left side of Fig. 19(b). As a result, the stress state is changed, leading to an extended loading path which actively postpones failure of the surrounded cementitious matrix. On the other hand, the positive Poisson's ratio honeycomb arrangement at the bottom exerts lateral compressive stress when loaded in tension. Hence, the failure state in the lower part of the composite is transferred from a kind of uniaxial tensile stress state to a mixed mode in the direction of uniaxial compression as depicted on the right side of Fig. 19(b). Again, changing the direction of loading yields a longer loading path that suspends failure. The driving factor behind the mechanism can be attributed to a mismatch in transverse strain between the cementitious matrix and the reinforcement that already occurs in the elastic regime (i.e., small strain) [16]. Similar to hoops in ordinary RC members, this causes arching confinement stresses as explained by Mander et al. [85]. In UD configurations, the exact opposite happens. The top chord of the reinforcement has a positive Poisson's ratio, resulting in lateral expansion under compressive strain, thereby pushing the failure state from uniaxial compression to a mixed mode in the direction of uniaxial tension. This shortens the loading path which increases the chance of matrix failure. In contrast, the bottom chord will be auxetic, providing lateral tensile stress when loaded in tension. As a consequence, the failure state is changed from uniaxial tensile towards a small biaxial tensile stress state, thus decreasing the strength and accelerating failure of the cementitious matrix. Future work, including simulations, will provide additional evidence of this hypothesized lateral confinement mechanism.

Fig. 20(a) shows that RE-UR significantly outperforms its constituents (i.e., REF+TPR) in terms of load capacity. For most of the other TPRCC specimens the overachievement is less pronounced, but approximately the same. Only RS-UD and TO-UD fail to overcome the combined load capacity from the individual constituent materials. Nevertheless, all UR configurations exhibit load capacity improvements compared to the summation of plain reference mortar and TPR load capacities. Fig. 20(b) illustrates that TO-UD yields toughness values that are unavailable from its separate components. Moreover, all TPRCC specimens exceed their contributor's joint toughness values.

Two properties used to compare the mechanical performance of the developed TPRCC specimens with literature are specific load capacity (δ in $\mathrm{kN\ mm^3/kg}$) and specific toughness (β in $\mathrm{kN\ mm^4/kg}$) as described

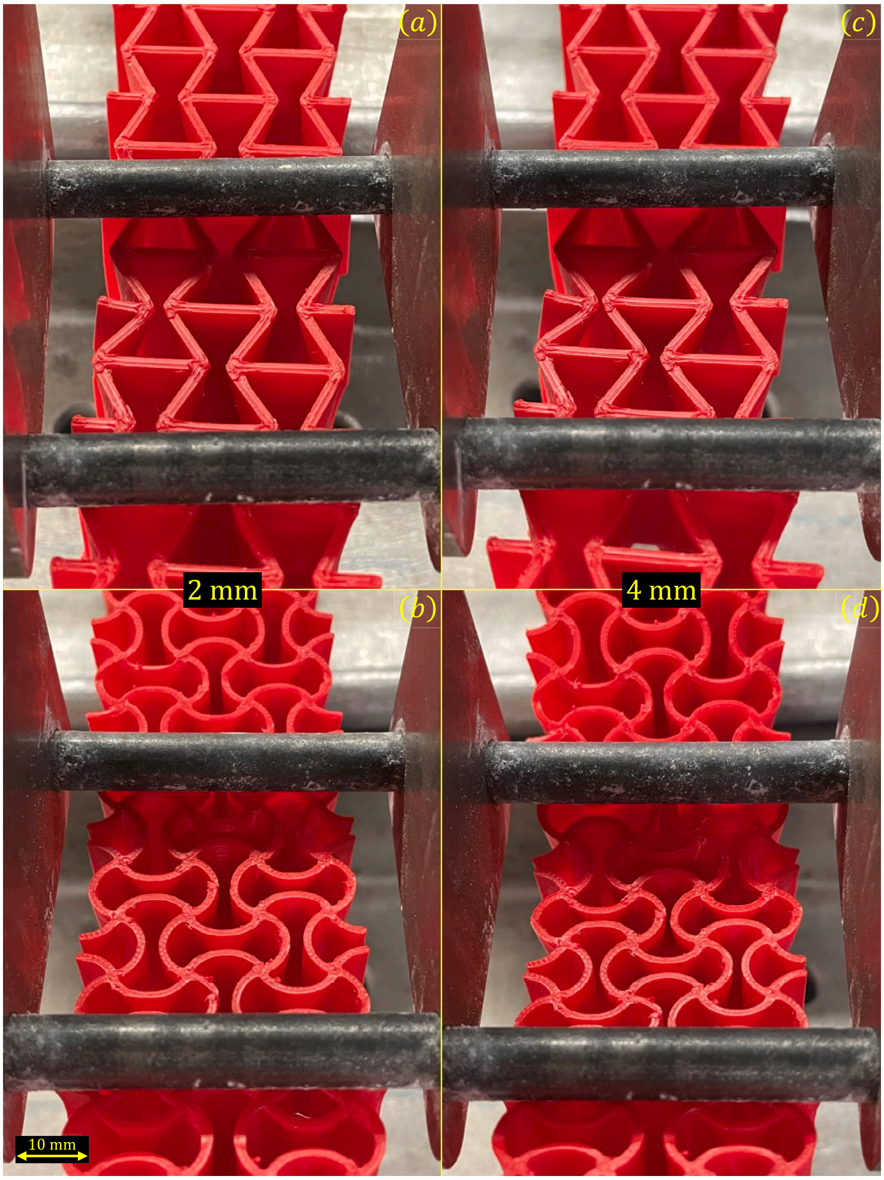

Fig. 14. Lateral contraction of TPR ABS 3D prints: (a,c) top views of RE-ABS-UR, (b,d) top views of TO-ABS-UR. Note: (a,b) 2 mm vertical displacement, (c,d) 4 mm vertical displacement.

by Barhemat et al. [74]. However, this is a comparison based on mass such that having a high volume of polymeric reinforcement inside cementitious composites will automatically yield higher specific properties. To illustrate the efficiency of the reinforcement methodologies, these values are normalized with respect to their volume fractions here:

$$\frac{\delta}{\rho} = \frac{S}{D}\frac{V}{V_\mathrm{r}}, \tag{1}$$

$$\frac{\beta}{\rho} = \frac{T}{D}\frac{V}{V_\mathrm{r}}, \tag{2}$$

where ρ is the reinforcement ratio, S the load capacity in kN, D the density of the composite in $\mathrm{kg\,mm^{-3}}$, V the volume of the composite in $\mathrm{mm^3}$, V_r the volume of the reinforcement in $\mathrm{mm^3}$, and T the toughness in J. Table 5 contains flexural data from various researchers as provided by Barhemat et al. [74], thereby only focusing on cementitious composites reinforced with polymeric reinforcement (i.e., APCC). All respective reinforcement ratios are provided accordingly. Nonetheless, different matrices, geometries and test setups may be used in the literature, such that the comparison presented here is indicative rather than definitive.

Table 5
Comparison between developed TPRCC specimens and literature.
Source: Adopted from [74].

Reference	δ (10^6 kN mm^3/kg)	β (10^6 kN mm^4/kg)	ρ	δ/ρ	β/ρ
RE-UR	3.80	7.76	0.147	25.9	52.8
RE-UD	2.70	7.72	0.147	18.4	52.5
RS-UR	2.37	6.48	0.146	16.2	44.4
RS-UD	1.32	4.10	0.146	9.04	28.1
TO-UR	2.25	9.99	0.146	15.4	68.4
TO-UD	1.74	15.1	0.146	11.9	103.4
APCC [6]	0.03	6.08	0.092	0.33	66.1
APCC [74]	9.04	22.0	0.807	11.2	27.3
APCC [75]	8.38	7.93	0.337	24.9	23.5
APCC [86]	6.87	5.15	0.305	22.5	16.9
APCC [87]	0.36	1.62	0.069	5.22	23.5

The CES plot in Fig. 21(a) shows the specific load capacity versus specific toughness for comparison, whilst Fig. 21(b) displays the same graph with all values normalized with respect to their volume fractions.

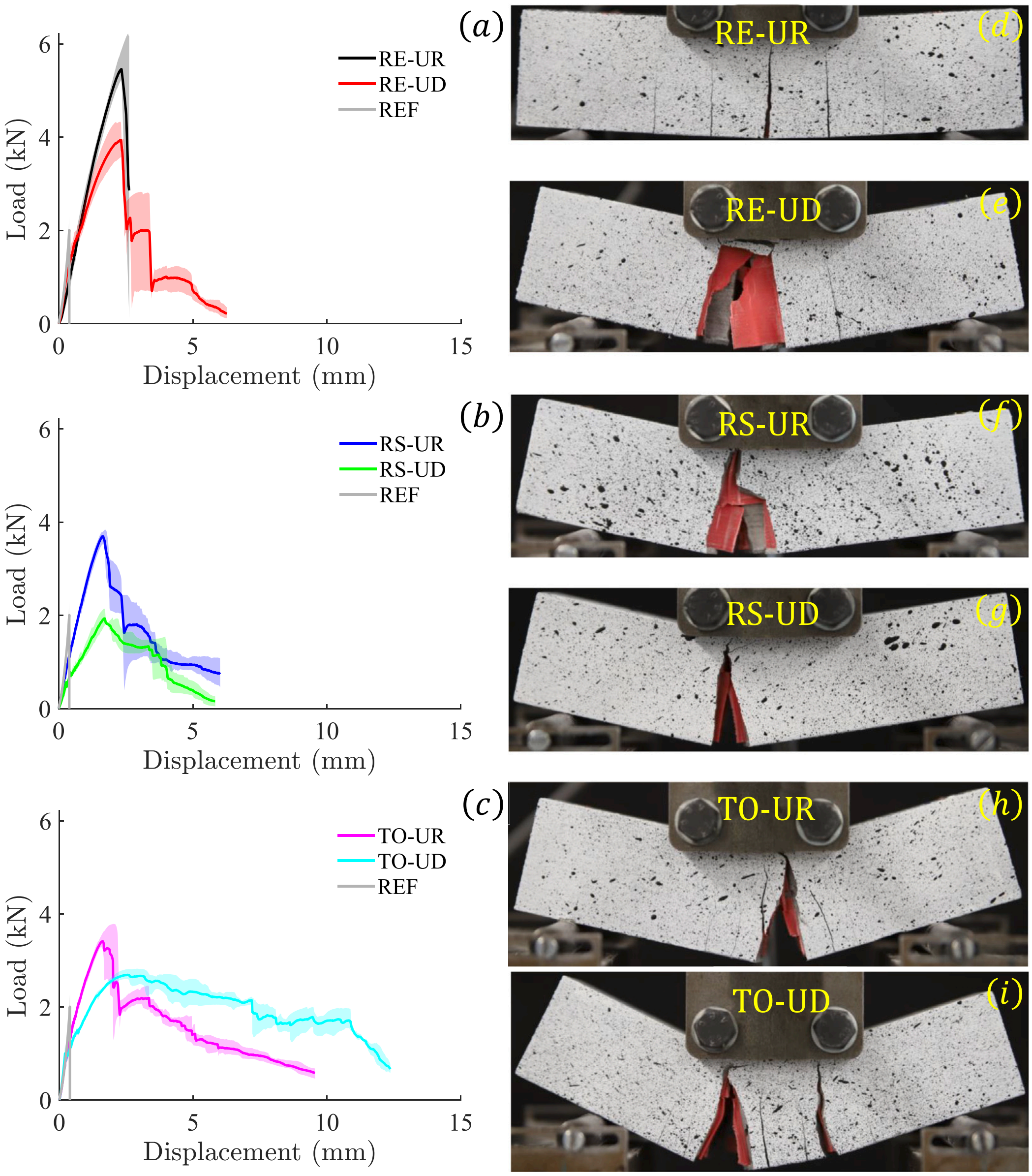

Fig. 15. Flexural behaviour of TPRCC specimens: (a–c) Load–displacement curves, (d–i) deformation and fracture patterns. Note: (d,f,h) UR, (e,g,i) UD. The shaded areas represent the variations across parallel testing, and the solid lines represent the average results.

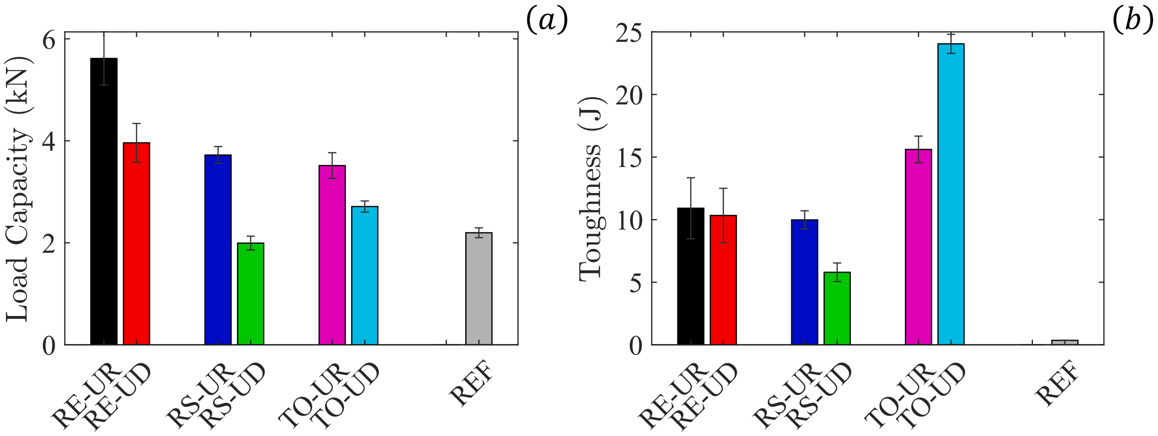

Fig. 16. Flexural properties of TPRCC specimens: (a) Load capacity, (b) toughness.

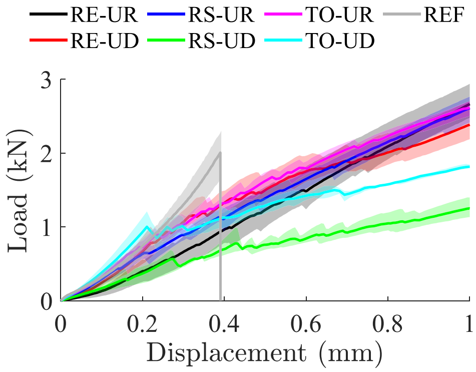

Fig. 17. First mm of TPRCC load–displacement curves indicating multiple cracking. The shaded areas represent the variations across parallel testing, and the solid lines represent the average results.

As depicted in Fig. 21(a), the APCC by Barhemat et al. [74] reaches a substantially high combination of specific load capacity and toughness, leaving all others far behind. Nonetheless, their design has a reinforcement ratio of about 80.7 %. When looking at the efficiency of the reinforcement strategy by normalizing these values with respect to the volume fraction (Fig. 21(b)), one can see that APCC [74] still showed a higher specific load capacity, but delivered a similar specific toughness compared to APCC [75] (ρ = 33.7 %) and RS-UD in this research (ρ = 14.6 %), despite a significantly higher reinforcement fraction.

Fig. 21(b) clearly shows that the developed TPRCC specimens are more efficient in terms of both load capacity and toughness. The TPR used in RE-UR turns out to be the most effective for load capacity, outperforming all other APCCs including those having significantly higher reinforcement ratios (i.e., 0.807, 0.337 and 0.305 versus 0.147 in [74,75,86] versus RE-UR, respectively, see Table 5). The TPR in TO layouts illustrate to be significantly more profitable for toughness, particularly TO-UD. Furthermore, Fig. 21(b) visualizes the trade-off between load capacity (e.g., RE-UR) and toughness (e.g., TO-UD), almost representing a Pareto front.

DIC analysis results for all TPRCC specimens are presented in Fig. 22. The images illustrate the cracking patterns prior to reaching peak load, with the coloured regions indicating localized horizontal strain. All layouts exhibited multiple cracking behaviour, although the specific crack patterns vary slightly. The RE-UR layout showed distinct, parallel cracks with uniform spacing (see Fig. 22(a)) which are likely reflections of the straight, vertical unit cell endings located right behind the longitudinal side surface as shown in Fig. 6. All other specimens displayed a denser arrangement of unevenly spaced cracks in the bent region. Among them, TO-UR (Fig. 22(e)) exhibited pronounced crack branching and deflection, primarily occurring near the height of the neutral axis. Although the cracking pattern of different layouts exhibit certain variations, the observed surface cracks are largely governed by the cracking and spalling behaviour of the outer mortar protective layer, which is approximately 2 mm thick. As a result, these surface features may not accurately represent the progression of internal damage within the composite. Therefore, the following section presents CT scanning results to identify key internal damage mechanisms and provide further insights into the behaviour of TPRCC.

Based on the four-point bending tests of the TPRCC specimens, the following flexural characteristics could be observed:

1. *Composite stiffness is barely impaired.* Compared to the plain reference mortar, the initial stiffness of most TPRCC configurations is not much affected by the significantly softer polymeric reinforcement phase. Moreover, the gradual increase in stiffness (and load capacity) occurs along the same trend as shown in Fig. 17.
2. *Multiple cracking achieved.* All tested samples exhibit multiple cracking behaviour, indicating their ability to redistribute bending stresses. This is evidenced by the small load drops in Fig. 17. RS has the least multiple cracking, which is directly related to toughness. RE shows increased multiple cracking and toughness. TO displays the most considerable amount of multiple cracks whilst maintaining a significantly higher toughness.
3. *The majority of composites outperform reference mortar.* All TPRCC specimens outperform the reference mortar in terms of load capacity, except for RS-UD reaching about the same value of 2 kN. Furthermore, all TPRCC layouts reach substantially larger toughness values than plain mortar.
4. *TPRCC-UR outperforms TPRCC-UD in load capacity for all reinforcement specimens.* The TPRCC-UR layouts have significantly higher load capacities with respect to their UD counterparts. Since the TPR ABS 3D prints exhibit comparable load capacities among UR and UD configurations, the difference in TPRCC-UR and TPRCC-UD load capacities are consistent with the hypothesized lateral confinement mechanism present in UR, which is absent in UD. TPRCC-UR specimens reach 73.8 %, 104.1 % and 45.2 % greater load capacities compared to UD configurations for RE, RS and TO, respectively.
5. *TO design shows exceptional toughness.* Especially TO-UD, which exhibits an increase in toughness of 6900 % with respect to the plain reference mortar. This relates to its consistent fracture pattern having two major cracks and the significant amount of intra-layer delamination observed in the 3D printed reinforcement.
6. *TPRCC yields significant improvements with respect to plain reference mortar.* Load capacity ratios yield improvements of 2.91, 1.80, 1.77 and 1.32 compared to the reference mortar for RE-UR, RS-UR, TO-UR and TO-UD, respectively. Similarly, toughness ratios display 35.41, 29.94, 48.07 and 70.00, respectively.
7. *TPRCC shows exceptional specific performance compared to literature.* The efficiency of the reinforcement methodologies is measured with respect to their volume factions. Based on reinforcement ratio, the TPRCC specimens developed in this work are more efficient in terms of both load capacity and toughness as shown in Fig. 21(b).
8. *Synergy between reinforcement and mortar.* Seeing that most flexural (auxetic) reinforcement applications in literature are compromising load capacity for considerable ductility at large deformations (i.e., in the Ultimate Limit State (ULS)), we rather focus on achieving synergistic composite action without clearly visible constituent separation at the Serviceability Limit State (SLS) for practical applications. This is evidenced by the continuous ascending curves before reaching the maximum load for all TPRCC specimens in Fig. 15.

3.2.2. CT scanning

The internal damage mechanisms of the composites were investigated via μ-CT scanning, as shown in the reconstructed images of the ROIs in Figs. 23 and 24. Top-view slices were extracted from heights corresponding to one-quarter (purple), one-half (green), and three-quarters (blue) of the specimen, while front-view slices (yellow) were taken along the central symmetry axis of the unit cell.

A comparison of the damage patterns in RE-UR and RE-UD at one-quarter height (Fig. 23(c) and (g)) reveals that in both cases, the TPR struts fractured. However, RE-UD exhibits more severe internal damage in the mortar matrix, with crack concentration observed particularly at the TPR corners. This phenomenon is attributed to the lateral expansion induced by the negative Poisson's ratio behaviour of the RE unit under tension. Such expansion intensifies at the corners, leading to stress concentration and consequent matrix cracking. In contrast, the mortar within the RE-UR cell remains largely intact, with no apparent macro-cracks. Debonding is limited to some TPR–mortar interfaces, likely

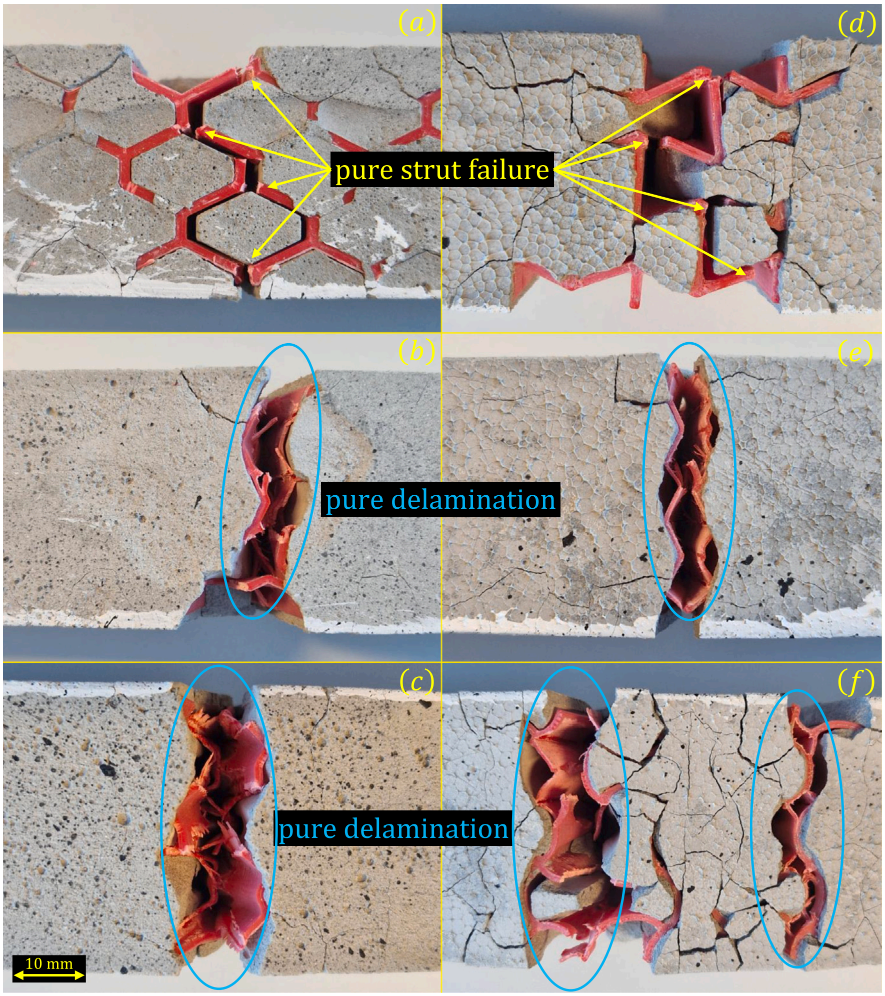

Fig. 18. Tensile surface images of TPRCC specimens after failure: (a) RE-UR, (b) RS-UR, (c) TO-UR, (d) RE-UD, (e) RS-UD, (f) TO-UD. Note: (a–c) bottom views of UR configurations, (d–f) bottom views of UD configurations.

caused by the minor contraction of the positive Poisson's ratio part under tension and the low bond strength between FDM 3D printed ABS and cementitious matrix [82]. Nevertheless, this lateral contraction introduces confining effects on the mortar, keeping it within the elastic range and subjecting it to a multi-axial tensile-compressive state (as shown in Fig. 19), which enhances the load-bearing capacity without inducing substantial plastic damage. At mid-height (Fig. 23(b) and (f)), RE-UD again demonstrates more pronounced mortar deterioration than RE-UR. This can be caused by the upward propagation of tensile cracks originating from the bottom, lacking constraint from the surrounding lattices.

Near the top of the specimen, mortar failure in RE-UD (Fig. 23(e)) diminishes, whereas RE-UR (Fig. 23(a)) begins to exhibit damage within the mortar. This trend can be understood in light of the evolving stress distribution during four-point bending. As the main crack propagates upward, the effective height of the beam decreases, causing the neutral axis to shift upward. Consequently, the auxetic region in RE-UR transitions from a purely compressive zone to a mixed-mode region with tension at the bottom and compression at the top. This induces lateral expansion in the lower tensile region, resulting in a damage morphology comparable to that observed in the lower part of RE-UD in Fig. 23(g). The failure patterns in both cases reflect the influence of the auxetic deformation mechanism.

The front-view slices further elucidate the contrasting damage evolution between RE-UR and RE-UD. In RE-UR (Fig. 23(d)), the TPR element undergoes noticeable fracture and lateral displacement near the neutral axis, with mortar cracking primarily initiating above the axis and propagating upward. Below the axis, the mortar remains virtually undamaged. This localization of failure in the negative Poisson's ratio zone aligns with earlier observations. Conversely, RE-UD (Fig. 23(h)) shows widespread cracking throughout the cementitious matrix along the specimen height. These μ-CT scanning analyses confirm that RE-UR more effectively confines internal damage compared to RE-UD, significantly mitigating matrix cracking and enhancing composite performance.

A similar failure mechanism is also observed in the TO group, as depicted in Fig. 24. While the dominant failure modes of TPRs differ, i.e., strut fracture in RE versus delamination in TO, the underlying TPR deformation behaviour and its role in mitigating matrix damage are consistent. Notably, the matrix in Fig. 24(a) shows less severe damage, potentially due to the fact that delamination of the ABS 3D printed reinforcement takes less force than the strut failure observed in Fig. 23(a).

4. Conclusions

In this study, the hypothesis is tested that Tailored Poisson's Ratio-reinforcement (TPR) causes a shift in the principal stress state of the cementitious matrix, thereby leading to an extended loading path in stress space, thereby actively postponing failure. Three Tailored Poisson's Ratio-reinforced Cementitious Composite (TPRCC) designs are developed and tested, leading to the following conclusions:

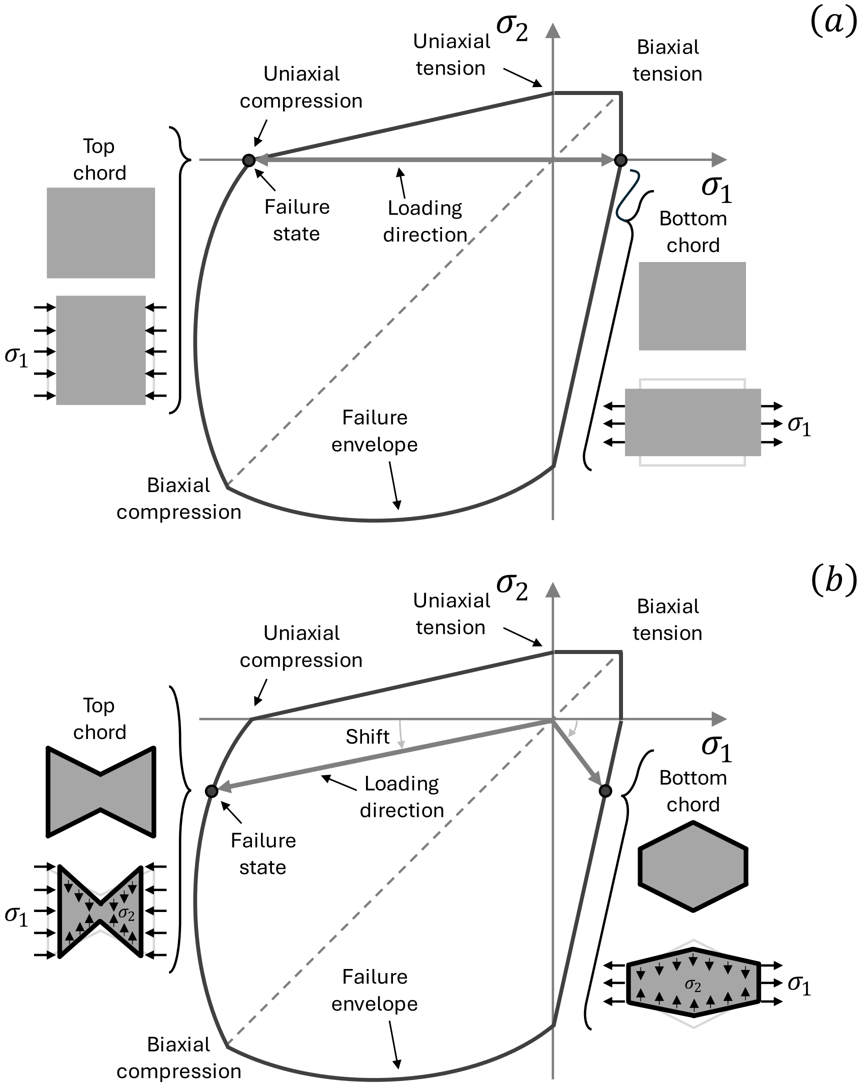

Fig. 19. Schematic representation of failure envelope for (a) plain reference mortar, and (b) RE-UR layout illustrating a conceptual, hypothesized shift in the principal stress state, leading to an extended loading path in stress space, actively postponing failure of the surrounded matrix.

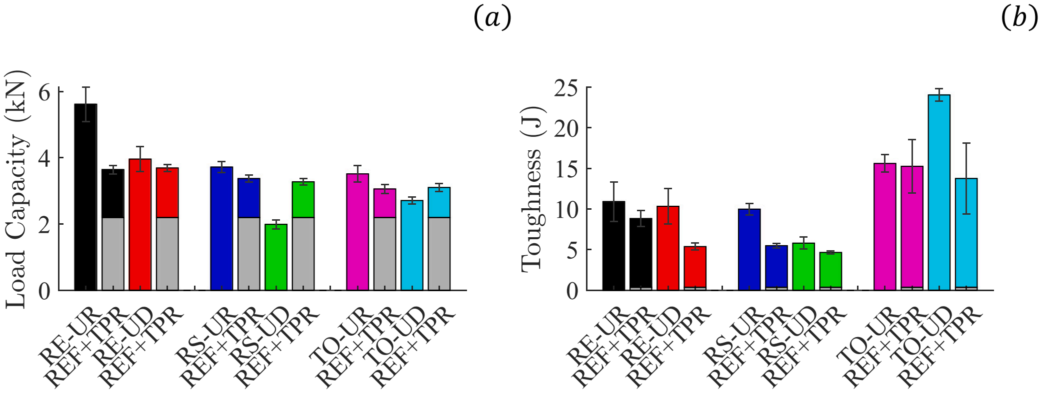

Fig. 20. Stacked flexural properties of TPRCC specimens: (a) Load capacity, (b) toughness. Note: Bars represented by REF+TPR comprise the joint response of plain reference mortar (REF) and TPR without cementitious matrix. Flexural properties of TPR and TPRCC are taken from Figs. 11 and 16.

1. *Reinforcement*: 3D-printed reinforcements with a prescribed gradient in Poisson's ratio suitable for flexural applications have been successfully designed and tested in bending. The resulting TPR 3D prints exhibit similar load capacities among UpRight (UR) and Upside Down (UD) configurations, despite their differences in horizontal cross-sectional area over the height. TPR

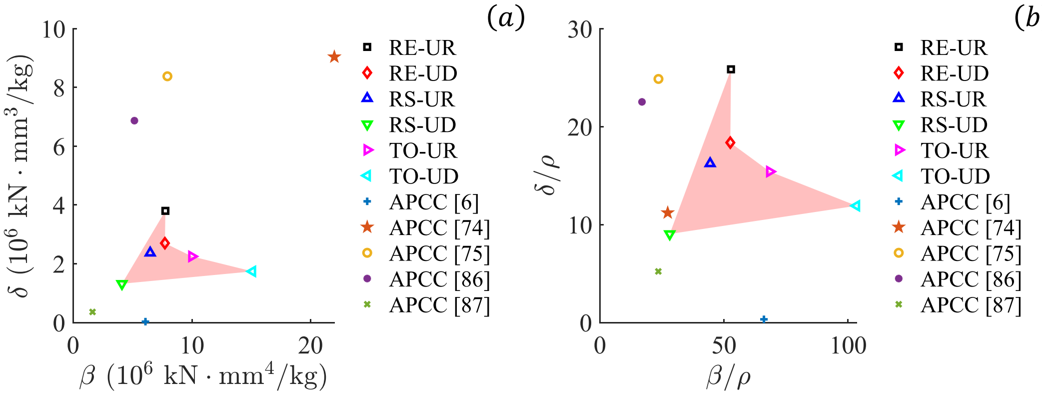

Fig. 21. Comparison of (a) specific load capacity (δ) and specific toughness (β), and (b) normalized with respect to reinforcement ratios (ρ) between developed TPRCC specimens and literature (adopted from [74]). The shaded area highlights the TPRCC specimens developed in this work.

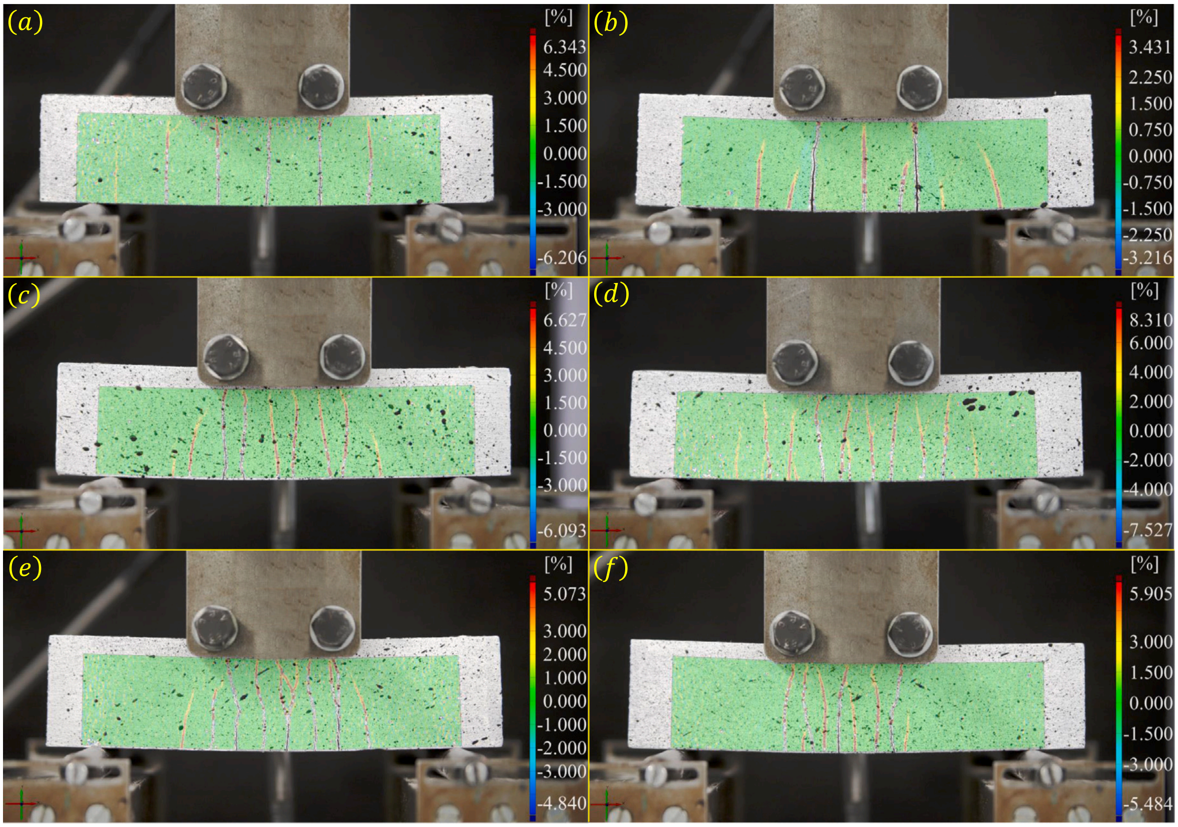

Fig. 22. DIC analysis images of TPRCC specimens before reaching peak load: (a) RE-UR, (b) RE-UD, (c) RS-UR, (d) RS-UD, (e) TO-UR, (f) TO-UD. Coloured regions indicate fine cracks or areas with concentrated horizontal strain. (For interpretation of the references to colour in this figure legend, the reader is referred to the web version of this article.)

load capacity and stiffness are positively associated with their strut thickness. In terms of toughness, TO significantly outperforms the others. The TPR load capacities can be related to the printing path-dependent anisotropy inherent to 3D printed polymers: Pure strut failure near stress concentrations exhibited the highest load capacity, whilst intra-layer delamination provided the lowest load-bearing capacity. Mixed failure modes provided intermediate values.

2. *Composite*: The hypothesized lateral confinement mechanism and its impact on load capacity and toughness have been evaluated in UR and UD configurations. TPRCC-UR layouts have significantly higher load capacities compared to their UD counterparts, yielding improvements of up to 191 % with respect to plain reference mortar. Since the TPR 3D prints exhibit comparable load capacities among UR and UD configurations, the difference in TPRCC-UR and TPRCC-UD load capacities are consistent with the hypothesized lateral confinement mechanism present in UR, which is absent in UD. This strongly supports the hypothesis that TPR causes a shift in the principal stress state, leading to an extended loading path in stress space, actively postponing failure of the surrounded matrix. However, lateral confinement remains a hypothesized mechanism because it is not directly quantified in this study. Confirmation requires simulations enabling full 3D stress analyses. Moreover, increases in energy absorption capacity of 6900 % compared to plain reference mortar are recorded.

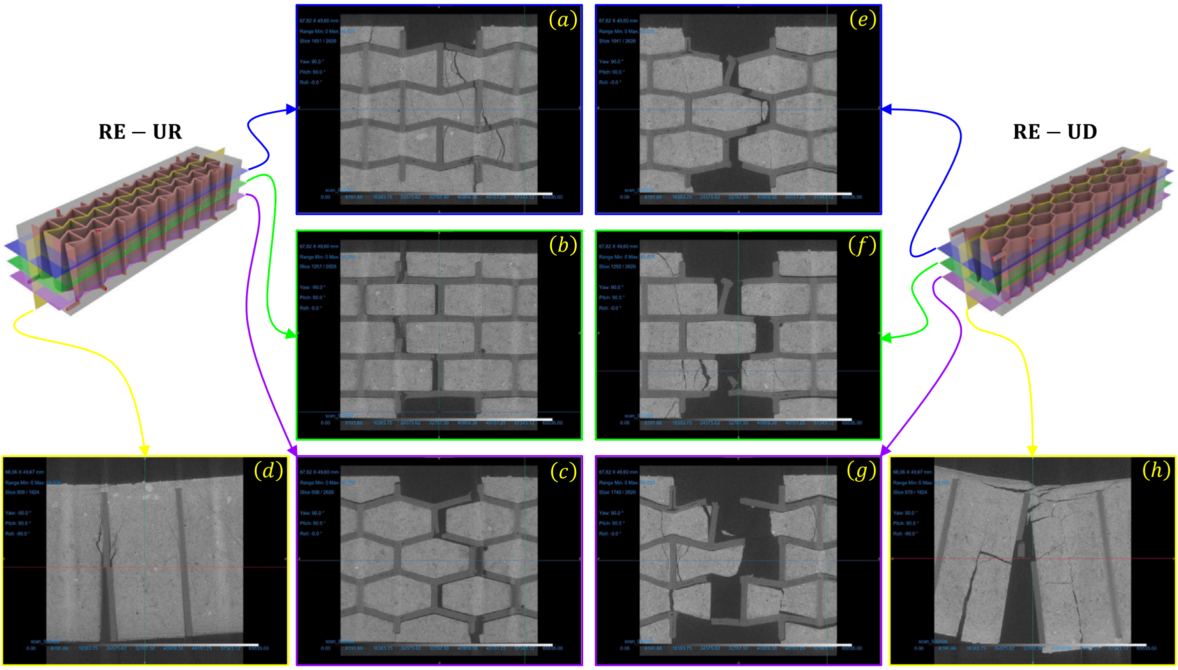

Fig. 23. Reconstructed μ-CT images of TPRCC: (a–d) RE-UR, and (e–h) RE-UD. (For interpretation of the references to colour in this figure legend, the reader is referred to the web version of this article.)

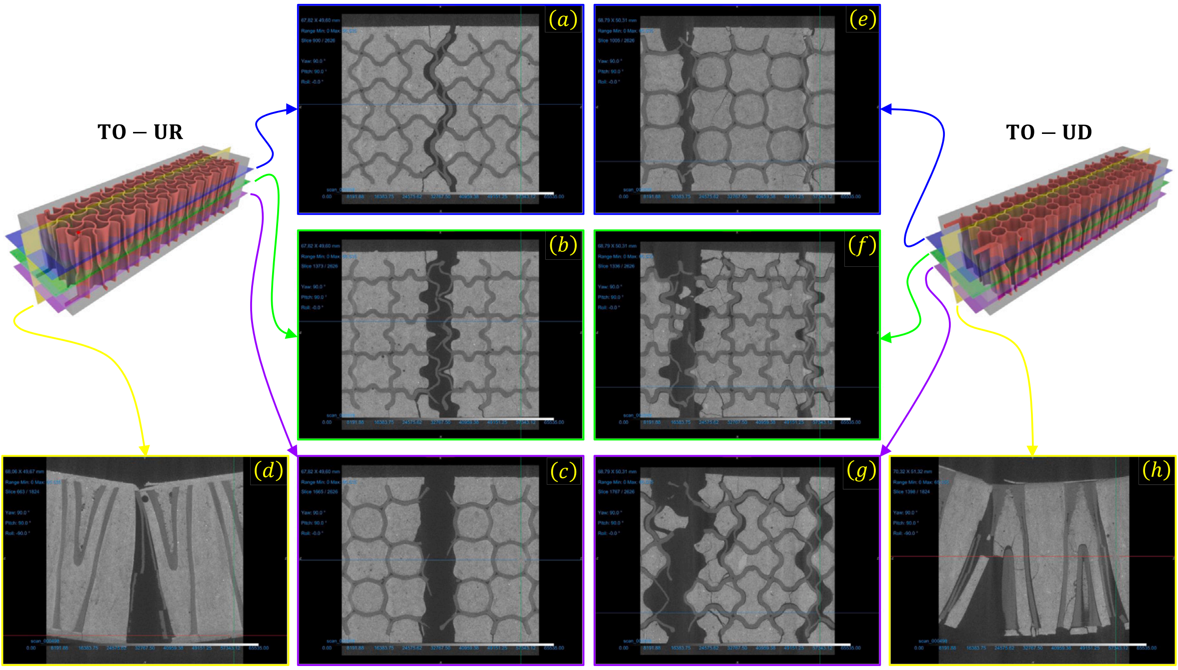

Fig. 24. Reconstructed μ-CT images of TPRCC: (a–d) TO-UR, and (e–h) TO-UD. (For interpretation of the references to colour in this figure legend, the reader is referred to the web version of this article.)

All tested samples exhibited multiple cracking behaviour, indicating their ability to redistribute bending stresses. Similarly, the TPRCC load capacities can be related to the printing path-dependent anisotropy of the 3D printed reinforcement: Pure strut failure reflected the highest load capacity, whilst vertical delamination is weaker. Nonetheless, the latter failure mode can be related to the astonishing gain in toughness for some of the TPRCC designs, albeit that the 3D printed reinforcement seems to be the limiting factor.

3. *Efficiency*: All TPRCC-UR configurations exhibit load capacity improvements compared to the summation of plain reference mortar and TPR load capacities. Moreover, all TPRCC specimens exceed their contributor's joint toughness values. Based on reinforcement ratio, the TPRCC designs developed in this work are more efficient in terms of both load capacity and toughness compared to other cementitious composites reinforced with polymeric reinforcement (i.e., APCC) in the literature. The TPR used in RE-UR turns out to be the most effective for load capacity, whilst the TPR in TO layouts illustrate to be significantly

more profitable for toughness, particularly TO-UD. However, there remains a trade-off between load capacity and toughness.

4. *Fracture*: μ-CT scanning confirms that TPRCC-UR more effectively mitigates internal damage compared to TPRCC-UD. In TPRCC-UD, mortar cracking is distributed throughout the specimen height, with the most severe damage occurring in the lower tensile zone due to lack of lateral confinement. In contrast, the lattices with a positive Poisson's ratio in the tensile zone of TPRCC-UR induce lateral contraction, effectively confining the mortar below the neutral axis and preventing significant damage. Minor matrix cracking is observed only in the upper region of the specimen, which can be attributed to the progressive upward shift of the neutral axis during loading. As a result, the auxetic lattices in TPRCC-UR begin to carry redistributed tensile stress, leading to lateral expansion and localized matrix damage in this region.
5. *Synergy*: All TPRCC designs developed in this work achieve synergistic composite action without clearly visible constituent separation at small deformations (i.e., Serviceability Limit State (SLS)). Further, the composite action already comes into play before significant matrix damage has occurred: All load displacement curves exhibit a continuous ascend until one distinct peak is reached, and only after that fracture progresses.
6. *Potential*: TPRCC designs provide great potential for up-scaling to practical applications. Based on the literature, polymeric reinforcements are favourable because of their low mass and high corrosion resistance, as well as the ability to apply 3D printing at larger scales. The latter is also true for metallic reinforcements. Further, the TPR 3D prints developed here are tailored according to the bending stress–strain distribution in beams, which is a common scenario in real-world load cases, making them financially viable. Finally, the synergistic composite action already present at small deformations enables its usability in cases where excessive deformations and crack widths need to be limited to prevent loss of the structure's durability (i.e., SLS).
7. *Limitations*: Given the exploratory nature of this work, several limitations must be acknowledged. For instance, the sample size per configuration is relatively small: Two for each TPR and three for each TPRCC. Larger number of specimens will allow for formal statistical analyses to substantiate and enhance the robustness of conclusions. Moreover, we focus on a single matrix type and a single filament material (Acrylonitrile Butadiene Styrene ((ABS)), which may limit generalization. It should also be noted that the Poisson's ratio distributions in the TPR 3D prints rely on analytical and topology optimized unit cell models, without direct experimental measurements. Further, lateral confinement remains a hypothesized mechanism because it is not directly quantified in this study. Confirmation requires simulations enabling full 3D stress analyses. Finally, scale effects, structural boundary conditions (e.g., in real beams or slabs) and durability assessments are not covered and require future studies.

5. Prospects

Even though the current work presented a novel reinforcement mechanism that shows a high degree of efficiency, synergy and potential practicality, it is important to identify remaining hurdles. To gain more insight in the composite interplay between TPR and cementitious matrix, some prospects for future research are listed below:

1. *Decreasing reinforcement ratio.* Although the present study considers relatively low reinforcement ratios (14.6 % to 14.7 %), it is believed that this amount can be (significantly) decreased to get closer to traditional reinforcement values. Optimization methods, such as topology optimization, present opportunities to further reduce volume fractions in TPRCC designs provided the increases in load capacity and toughness are maintained. For instance, material could be removed from low stress regions by following examples from construction practice (e.g., perforated beams). This needs to be studied further, because it could improve the bond behaviour of the composites as the cementitious matrix would be interconnected among the unit cells. The current TPRCC designs solely rely on the bond between the cementitious matrix and 3D printed reinforcement, which is shown to be weak.
2. *Exploring other reinforcing materials.* Acrylonitrile Butadiene Styrene (ABS) is a relatively strong and stiff polymer filament that is compatible with Fused Deposition Modelling (FDM) 3D printing. However, there are many more filaments to choose from that have better inter-layer adhesion than ABS, such as Thermoplastic PolyUrethane (TPU). Additionally, various AM techniques besides FDM enable the construction of polymeric and metallic reinforcements, such as StereoLithogrAphy (SLA), Powder Bed Fusion (PBF) or Selective Laser Sintering (SLS). These processes could mitigate the printing path-dependent anisotropy present in FDM 3D printed polymers. Another approach might be the Lost Mould Technique (LMT), which makes use of FDM to create a model of the reinforcement. Metallic reinforcements would also be stronger and stiffer compared to their polymeric counterparts.
3. *Practical considerations.* Several issues related to the reinforcement manufacturing technique (FDM) need to be addressed, such as inter-layer failure among stacked layers and long printing times. Regarding up-scaling, industrial 3D printers do exist, albeit printing times may grow even larger. Moreover, scale effects and structural boundary conditions (e.g., in real beams or slabs) are not covered and require future studies.
4. *Comparison with traditional reinforcement.* To truly evaluate the efficiency and potential of TPRCC with respect to construction practice, comparisons with traditionally reinforced cementitious composites on the same scale are needed using similar reinforcing material (i.e., ABS). Only then will the real potential be uncovered before proceeding towards up-scaling.
5. *Numerical modelling.* Simulations in future work will provide fully confirming evidence of the hypothesized lateral confinement mechanism. These will enable visualization of principal stress states in the cementitious matrix, thereby proving the occurrence of lateral confinement prior to reinforcement failure. Additionally, simulated cracking patterns may be compared with CT scans for validation purposes.

CRediT authorship contribution statement

Rowin J.M. Bol: Writing – original draft, Visualization, Validation, Software, Resources, Methodology, Investigation, Formal analysis, Data curation, Conceptualization. **Wen Zhou:** Writing – original draft, Investigation, Formal analysis. **Zhaozheng Meng:** Writing – review & editing. **Erik Schlangen:** Writing – review & editing, Supervision. **Branko Šavija:** Writing – review & editing, Supervision, Resources, Project administration, Funding acquisition.

Declaration of competing interest

The authors declare the following financial interests/personal relationships which may be considered as potential competing interests: Branko Savija reports financial support was provided by European Research Council. If there are other authors, they declare that they have no known competing financial interests or personal relationships that could have appeared to influence the work reported in this paper.

Acknowledgements

The authors would like to sincerely thank our valuable technicians, Maiko van Leeuwen and Arjan Thijssen, for their assistance with mechanical testing and CT scanning, respectively. Rowin J.M. Bol, Wen Zhou, Zhoazheng Meng & Branko Šavija acknowledge the financial support of the European Research Council (ERC) within the framework of the ERC Starting Grant Project 'Auxetic Cementitious Composites by 3D printing (ACC-3D)', Grant Agreement Number 101041342. The funding source was not involved in the content of this work.

Data availability

Data will be made available on request.

References

[1] E.O. Momoh, A. Jayasinghe, M. Hajsadeghi, R. Vinai, K.E. Evans, P. Kripakaran, J. Orr, A state-of-the-art review on the application of auxetic materials in cementitious composites, Thin-Walled Struct. 196 (2024) 111447, [Online]. Available: https://linkinghub.elsevier.com/retrieve/pii/S0263823123009254.

[2] C. Tang, J. Liu, W. Hao, Y. Wei, Flexural properties of 3D printed graded lattice reinforced cementitious composites using digital image correlation, Mater. Des. 227 (2023).

[3] W. Hao, J. Liu, H. Kanwal, Compressive properties of cementitious composites reinforced by 3D printed PA 6 lattice, Polym. Test. 117 (2023).

[4] E. Etemadi, M. Hosseinabadi, F. Scarpa, H. Hu, Design, FDM printing, FE and theoretical analysis of auxetic structures consisting of arc-shaped and dumbell-shaped struts under quasi-static loading, Compos. Struct. 326 (2023).

[5] A. Bouteldja, M.A. Louar, L. Hemmouche, L. Gilson, A. Miranda-Vicario, L. Rabet, Experimental investigation of the quasi-static and dynamic compressive behavior of polymer-based 3D-printed lattice structures, Int. J. Impact Eng. 180 (2023).

[6] Y. Xu, B. Šavija, Development of strain hardening cementitious composite (SHCC) reinforced with 3D printed polymeric reinforcement: Mechanical properties, Compos. Part B: Eng. 174 (2019).

[7] Y. Xu, Z. Meng, R.J.M. Bol, B. Šavija, Spring-like behavior of cementitious composite enabled by auxetic hyperelastic frame, Int. J. Mech. Sci. 275 (2024).

[8] R.J.M. Bol, B. Šavija, Micromechanical models for FDM 3D-printed polymers: A review, Polymers 15 (2023) 4497, [Online]. Available: https://www.mdpi.com/2073-4360/15/23/4497.

[9] R.J.M. Bol, Y. Xu, B. Šavija, Printing path-dependent two-scale models for 3D printed planar auxetics by material extrusion, Addit. Manuf. 89 (2024).

[10] U.A. Dar, H.H. Mian, M. Abid, A. Topa, M.Z. Sheikh, M. Bilal, Experimental and numerical investigation of compressive behavior of lattice structures manufactured through projection micro stereolithography, Mater. Today Commun. 25 (2020).

[11] J. Zhang, X. Chen, Y. Sun, Y. Wang, L. Bai, Sound-absorption and mechanical properties of multisheet gyroid lattice structures by stereolithography, Compos. Struct. 325 (2023).

[12] J.H. Kang, K. Sakthiabirami, K.J. Jang, J.G. Jang, G.J. Oh, C. Park, J.G. Fisher, S.W. Park, Mechanical and biological evaluation of lattice structured hydroxyapatite scaffolds produced via stereolithography additive manufacturing, Mater. Des. 214 (2022).

[13] R. Raj, M.J. Prajapati, J.T. Tsai, A. Kumar, J.Y. Jeng, Design and additive manufacturing of novel hybrid lattice metamaterial for enhanced energy absorption and structural stability, Mater. Des. 245 (2024).

[14] R. Rodríguez-Aparicio, J.M. Alegre, W.M. Verbeeten, M. Lorenzo-Bañuelos, I.I. Cuesta, Methodology to predict mechanical properties of PA-12 lattice structures manufactured by powder bed fusion, Addit. Manuf. 78 (2023).

[15] S. Li, T. Wang, S. Chen, Y. Li, Y. Zou, B. Cao, J. Hu, X. Tan, B. Wang, Compressive properties and biocompatibility of additively manufactured lattice structures by using bioactive materials, Thin-Walled Struct. 205 (2024).

[16] T. Vitalis, A. Gross, G. Tzortzinis, B. Schagen, S. Gerasimidis, Enhancing mortar composite matrices with three-dimensional auxetic truss lattice materials for reinforced concrete structures, Constr. Build. Mater. 457 (2024).

[17] P. Dong, J. Hu, C. Lin, W. Ding, J. Liu, Y. Liu, Topology-optimized lattice enhanced cementitious composites, Mater. Des. 244 (2024).

[18] A. Clausen, F. Wang, J.S. Jensen, O. Sigmund, J.A. Lewis, Topology optimized architectures with programmable Poisson's ratio over large deformations, Adv. Mater. 27 (2015) 5523–5527.

[19] L. Stepinac, J. Galić, Preliminary investigation of the large-scale sandwich decks with graded 3D printed auxetic core, J. Sandw. Struct. Mater. 27 (2025) 260–278, [Online]. Available: https://journals.sagepub.com/doi/10.1177/10996362241298144.

[20] A. Panesar, M. Abdi, D. Hickman, I. Ashcroft, Strategies for functionally graded lattice structures derived using topology optimisation for additive manufacturing, Addit. Manuf. 19 (2018) 81–94.

[21] Y. Xu, H. Zhang, Y. Gan, B. Šavija, Cementitious composites reinforced with 3D printed functionally graded polymeric lattice structures: Experiments and modelling, Addit. Manuf. 39 (2021).

[22] Z. Meng, Y. Xu, J. Xie, W. Zhou, R.J.M. Bol, Q. feng Liu, B. Šavija, Unraveling the reinforcing mechanisms for cementitious composites with 3D printed multidirectional auxetic lattices using X-ray computed tomography, Mater. Des. 246 (2024) 113331, [Online]. Available: https://linkinghub.elsevier.com/retrieve/pii/S0264127524007068.

[23] Y. Xu, B. Šavija, Auxetic cementitious composites (ACCs) with excellent compressive ductility: Experiments and modeling, Mater. Des. 237 (2024) 112572, [Online]. Available: https://linkinghub.elsevier.com/retrieve/pii/S0264127523009887.

[24] T.C. Lim, Analogies across auxetic models based on deformation mechanism, Phys. Status Solidi Rapid Res. Lett. 11 (2017).

[25] J.J. Warner, A.R. Gillies, H.H. Hwang, H. Zhang, R.L. Lieber, S. Chen, 3D-printed biomaterials with regional auxetic properties, J. Mech. Behav. Biomed. Mater. 76 (2017) 145–152.

[26] S. Maran, I.G. Masters, G.J. Gibbons, Additive manufacture of 3d auxetic structures by laser powder bed fusion—design influence on manufacturing accuracy and mechanical properties, Appl. Sci. (Switz.) 10 (2020) 1–19.

[27] M.S. Rad, Y. Prawoto, Z. Ahmad, Analytical solution and finite element approach to the 3D re-entrant structures of auxetic materials, Mech. Mater. 74 (2014) 76–87.

[28] A. Joseph, V. Mahesh, D. Harursampath, On the application of additive manufacturing methods for auxetic structures: a review, Adv. Manuf. 9 (2021) 342–368.

[29] K.E. Evans, A. Alderson, Auxetic materials: Functional materials and structures from lateral thinking!, Adv. Mater. 12 (2000) 617–628.

[30] V.A. Lvov, F.S. Senatov, A.A. Stepashkin, A.A. Veveris, M.D. Pavlov, A.A. Komissarov, Low-cycle fatigue behavior of 3D-printed metallic auxetic structure, Mater. Today: Proc. 33 (2020) 1979–1983.

[31] C.-H. Hsueh, S. Schmauder, C.-S. Chen, K.K. Chawla, N. Chawla, W. Chen, Y. Kagawa, Handbook of Mechanics of Materials, Springer Nature Singapore Pte Ltd, 2019.

[32] J. Carlos, A. Elipe, A.D. Lantada, Comparative study of auxetic geometries by means of computer-aided design and engineering, Smart Mater. Struct. 21 (2012).

[33] H.M. Kolken, K. Lietaert, T. van der Sloten, B. Pouran, A. Meynen, G.V. Loock, H. Weinans, L. Scheys, A.A. Zadpoor, Mechanical performance of auxetic meta-biomaterials, J. Mech. Behav. Biomed. Mater. 104 (2020).

[34] X.T. Wang, B. Wang, X.W. Li, L. Ma, Mechanical properties of 3D re-entrant auxetic cellular structures, Int. J. Mech. Sci. 131–132 (2017) 396–407.

[35] T. Li, Y. Chen, X. Hu, Y. Li, L. Wang, Exploiting negative Poisson's ratio to design 3D-printed composites with enhanced mechanical properties, Mater. Des. 142 (2018) 247–258.

[36] Y. Xu, H. Zhang, E. Schlangen, M. Luković, B. Šavija, Cementitious cellular composites with auxetic behavior, Cem. Concr. Compos. 111 (2020).

[37] Y. Xu, E. Schlangen, M. Luković, B. Šavija, Tunable mechanical behavior of auxetic cementitious cellular composites (CCCs): Experiments and simulations, Constr. Build. Mater. 266 (2021).

[38] X. Li, W. Peng, W. Wu, J. Xiong, Y. Lu, Auxetic mechanical metamaterials: from soft to stiff, 2023.

[39] R. Lakes, Foam structures with a negative Poisson's ratio, Science 235 (1987) 1038–1040, [Online]. Available: www.sciencemag.org.

[40] K.E. Evans, Auxetic polymers: a new range of materials, Endeavour 15 (1991) 170–174.

[41] T. Young, A Course of Lectures on Natural Philosophy and the Mechanical Arts, vol. II, Printed for J. Johnson, London, 1807.

[42] A. Love, A Treatise on the Mathematical Theory of Elasticity, vol. 1, Cambridge University Press, Cambridge, 1892, [Online]. Available: https://hal.science/hal-01307751.

[43] J. Wu, O. Sigmund, J.P. Groen, Topology optimization of multi-scale structures: a review, 2021, pp. 1455–1480.

[44] X. Xue, C. Lin, F. Wu, Z. Li, J. Liao, Lattice structures with negative Poisson's ratio: A review, 2023.

[45] Y. Xu, Architected cementitious cellular materials towards auxetic behavior, 2021, http://dx.doi.org/10.4233/uuid:1a9e29a6-4868-4096-bc88-a1095cf568d3, [Online]. Available.

[46] I.G. Masters, K.E. Evans, Models for the elastic deformation of honeycombs, Compos. Struct. 35 (1996) 403–422.

[47] L.J. Gibson, Cellular solids, MRS Bull. 28 (2003) 270–274.

[48] M. Awasthi, S. Naskar, A. Singh, T. Mukhopadhyay, Constitutive behavior of asymmetric multi-material honeycombs with bi-level variably-thickened composite architecture, Thin-Walled Struct. 203 (2024).

[49] X.C. Teng, X. Ren, Y. Zhang, W. Jiang, Y. Pan, X.G. Zhang, X.Y. Zhang, Y.M. Xie, A simple 3D re-entrant auxetic metamaterial with enhanced energy absorption, Int. J. Mech. Sci. 229 (2022).

[50] L. Yang, O. Harrysson, H. West, D. Cormier, Mechanical properties of 3D re-entrant honeycomb auxetic structures realized via additive manufacturing, Int. J. Solids Struct. 69–70 (2015) 475–490.
[51] W. Liu, N. Wang, T. Luo, Z. Lin, In-plane dynamic crushing of re-entrant auxetic cellular structure, Mater. Des. 100 (2016) 84–91.
[52] C. Zmuda, Design of structural composite with auxetic behavior, 2017, [Online]. Available: http://www.wpi.edu/Academics/Projects.
[53] Y. Yao, L. Wang, J. Li, S. Tian, M. Zhang, Y. Fan, A novel auxetic structure based bone screw design: Tensile mechanical characterization and pullout fixation strength evaluation, Mater. Des. 188 (2020).
[54] G.A. Lyngdoh, N.K. Kelter, S. Doner, N.M. Krishnan, S. Das, Elucidating the auxetic behavior of cementitious cellular composites using finite element analysis and interpretable machine learning, Mater. Des. 213 (2022).
[55] X. Ren, J. Shen, P. Tran, T.D. Ngo, Y.M. Xie, Auxetic nail: Design and experimental study, Compos. Struct. 184 (2018) 288–298.
[56] T.A. Schaedler, W.B. Carter, Architected cellular materials, Annu. Rev. Mater. Res. 46 (2016) 187–210.
[57] M. Asad, M. Dhanasekar, T. Zahra, D. Thambiratnam, Impact mitigation of masonry walls with carbon fibre and auxetic fibre composite renders – A numerical study, Structures 28 (2020) 2733–2751.
[58] X.G. Zhang, W. Jiang, Y. Zhang, C. Luo, X.Y. Zhang, D. Han, J. Hao, X.C. Teng, Y.M. Xie, X. Ren, Energy absorption properties of composite tubes with hexagonal and re-entrant honeycomb fillers, Constr. Build. Mater. 356 (2022).
[59] F. Scarpa, L.G. Ciffo, J.R. Yates, Dynamic properties of high structural integrity auxetic open cell foam, Smart Mater. Struct. 13 (2004) 49–56.
[60] S. Yang, C. Qi, D. Wang, R. Gao, H. Hu, J. Shu, A comparative study of ballistic resistance of sandwich panels with aluminum foam and auxetic honeycomb cores, Adv. Mech. Eng. 2013 (2013).
[61] P. Subramani, S. Rana, D.V. Oliveira, R. Fangueiro, J. Xavier, Development of novel auxetic structures based on braided composites, Mater. Des. 61 (2014) 286–295.
[62] T. Zahra, M. Dhanasekar, Characterisation of cementitious polymer mortar – Auxetic foam composites, Constr. Build. Mater. 147 (2017) 143–159.
[63] N. Novak, L. Krstulović-Opara, Z. Ren, M. Vesenjak, Compression and shear behaviour of graded chiral auxetic structures, Mech. Mater. 148 (2020).
[64] G. Zhao, Y. Fan, C. Tang, Y. Wei, W. Hao, Preparation and compressive properties of cementitious composites reinforced by 3D printed cellular structures with a negative Poisson's ratio, Dev. Built Environ. 17 (2024).
[65] N.K. Choudhry, T.K. Nguyen, V. Nguyen-Van, B. Panda, P. Tran, Auxetic lattice reinforcement for tailored mechanical properties in cementitious composite: Experiments and modelling, Constr. Build. Mater. 438 (2024).
[66] G. Tzortzinis, A. Gross, S. Gerasimidis, Auxetic boosting of confinement in mortar by 3D reentrant truss lattices for next generation steel reinforced concrete members, Extrem. Mech. Lett. 52 (2022).
[67] M. Chen, Z. Chen, Y. Xuan, T. Zhang, M. Zhang, Static and dynamic compressive behaviour of 3D printed auxetic lattice reinforced ultra-high performance concrete, Cem. Concr. Compos. 139 (2023).
[68] T. Zahra, M. Asad, J. Thamboo, Flexural behaviour of cementitious composites embedded with 3D printed re-entrant chiral auxetic meshes, Smart Mater. Struct. 33 (2024).
[69] B. Xie, R. Tian, H. Zhao, T. Ye, Y. Zhang, N. Hu, Controlling crack propagation in layered beams with architected lattice-reinforced composite interlayer designs, Constr. Build. Mater. 426 (2024).
[70] J.A. Rosewitz, H.A. Choshali, N. Rahbar, Bioinspired design of architected cement-polymer composites, Cem. Concr. Compos. 96 (2019) 252–265.
[71] D. Edmund, T. Zahra, M. Asad, J. Thamboo, Experimental investigation on tensile characteristics of 3D printed auxetic embedded cementitious composites and shear bonding behaviour to masonry, J. Build. Eng. 97 (2024).
[72] S. Pichandi, Universidade do minho escola de engenharia development of composite auxetic structures for civil engineering applications, 2016.
[73] J. Liu, H. Kanwal, C. Tang, W. Hao, Study on flexural properties of 3D printed lattice-reinforced concrete structures using acoustic emission and digital image correlation, Constr. Build. Mater. 333 (2022).
[74] R. Barhemat, S. Mahjoubi, W. Meng, Y. Bao, Automated design of architectured polymer-concrete composites with high specific flexural strength and toughness using sequential learning, Constr. Build. Mater. 449 (2024).
[75] B. Salazar, P. Aghdasi, I.D. Williams, C.P. Ostertag, H.K. Taylor, Polymer lattice-reinforcement for enhancing ductility of concrete, Mater. Des. 196 (2020).
[76] B. Xie, X. Li, X. Zhao, N. Hu, Tunable properties and responses of architected lattice-reinforced cementitious composite components induced by versatile cell topology and distributions, Compos. Struct. 312 (2023).
[77] S. Qin, S. Cao, E. Yilmaz, J. Li, Influence of types and shapes of 3D printed polymeric lattice on ductility performance of cementitious backfill composites, Constr. Build. Mater. 307 (2021).
[78] P. Dong, W. Ding, H. Yuan, Q. Wang, 3D-printed polymeric lattice-enhanced sustainable municipal solid waste incineration fly ash alkali-activated cementitious composites, Dev. Built Environ. 12 (2022).
[79] W. Zhou, R.J. Bol, Y. Zhou, Z. Meng, Y. Xu, J. Xie, B. Šavija, Reinforcing mechanism of lattice-reinforced cementitious composites: insights into flexural performance and material interactions, Mater. Des. 256 (2025) 114332, [Online]. Available: https://linkinghub.elsevier.com/retrieve/pii/S026412752500752X.
[80] S. Askarinejad, H.A. Choshali, C. Flavin, N. Rahbar, Effects of tablet waviness on the mechanical response of architected multilayered materials: Modeling and experiment, Compos. Struct. 195 (2018) 118–125.
[81] Y. Xu, Z. Wan, B. Šavija, Elevating mechanical performance of cementitious composites with surface-modified 3D-printed polymeric reinforcements, Dev. Built Environ. 19 (2024).
[82] R.J.M. Bol, Y. Xu, M. Luković, B. Šavija, Does printing direction influence the bond between 3D printed polymeric reinforcement and cementitious matrix? Eng. Fail. Anal. 174 (2025) 109471, [Online]. Available: https://linkinghub.elsevier.com/retrieve/pii/S1350630725002122.
[83] Z. Lu, Q. Wang, X. Li, Z. Yang, Elastic properties of two novel auxetic 3D cellular structures, Int. J. Solids Struct. 124 (2017) 46–56.
[84] F. Wang, O. Sigmund, J.S. Jensen, Design of materials with prescribed nonlinear properties, J. Mech. Phys. Solids 69 (2014) 156–174.
[85] J.B. Mander, M.J.N. Priestley, R. Park, Theoretical stress-strain model for confined concrete, J. Struct. Eng. 114 (1988) 1804–1826.
[86] B. Salazar, I. Williams, P. Aghdasi, C. Ostertag, H. Taylor, Bending and crack characteristics of polymer lattice-reinforced mortar, 2018, pp. 261–266.
[87] I. Farina, F. Fabbrocino, G. Carpentieri, M. Modano, A. Amendola, R. Goodall, L. Feo, F. Fraternali, On the reinforcement of cement mortars through 3D printed polymeric and metallic fibers, Compos. Part B: Eng. 90 (2016) 76–85.